Research Square

Preprints are preliminary reports that have not undergone peer review.
They should not be considered conclusive, used to inform clinical practice,
or referenced by the media as validated information.

CREB3L1 regulates mitochondrial bioenergetics and cytoskeletal remodeling during axon specification in developing neurons

Cecilia Alvarez

ceci.alvarez@unc.edu.ar

Universidad Nacional de Córdoba https://orcid.org/0000-0001-9135-7272

Victoria Rozes

CIBICI-CONICET-UNC

Carlos Wilson

Centro de Investigación en Medicina Traslacional Severo R. Amuchástegui (CIMETSA) Instituto Universitario de Ciencias Biomédicas de Córdoba

Raffaella De Pace

NIH https://orcid.org/0000-0002-8179-6869

Valentín Marrupe

Facultad de Ciencias Quimicas. CIBICI-CONICET-UNC

Brandon Fuller

Eunice Kennedy Shriver National Institute of Child Health and Human Development, National Institutes of Health https://orcid.org/0009-0003-7885-4145

Mira Sohn

National Institutes of Health https://orcid.org/0009-0000-1929-9856

Ryan Dale

National Institutes of Health https://orcid.org/0000-0003-2664-3744

Tianwei Li

National Institutes of Health

Emilia Hisse

Facultad de Ciencias Quimicas. CIBICI-CONICET-UNC

Ana Flores Guirado

Universidad Nacional de Córdoba-CIBICI-CONICET.

Luciana Sampieri

Facultad de Ciencias Quimicas. CIBICI-CONICET-UNC https://orcid.org/0000-0002-1269-4463

Nicolas Nunez

University of Zurich https://orcid.org/0000-0003-3837-270X

Cecilia Conde

Instituto Ferreyra (INIMEC-CONICET-UNC), Instituto Uniuversitario Ciencias Biomedicas Cordoba (IUCBC)

Juan Bonifacino

National Institutes of Health https://orcid.org/0000-0002-5673-6370

Article

Keywords: CREB3L1, transcription factor, neurons, neuronal differentiation, gene regulation, i3Neurons, mitochondrial function

Posted Date: September 23rd, 2026

DOI: https://doi.org/10.21203/rs.3.rs-10961853/v1

License: This work is licensed under a Creative Commons Attribution 4.0 International License. Read Full License

Additional Declarations: There is **NO** Competing Interest.

CREB3L1 regulates mitochondrial bioenergetics and cytoskeletal remodeling during axon specification in developing neurons

Victoria Rozés-Salvador[1,2]*, Carlos Wilson[2,3], Raffaela De Pace[4], Valentín Marrupe[1], Brandon Fuller[5], Mira Sohn[5], Ryan K Dale[5], Tianwei Li[6], Emilia Hisse[1,2], Ana Paula Flores Guirado[1,2], Luciana Sampieri[1,2], Nicolás Núñez[1,2], Cecilia Conde[2,7], Juan S. Bonifacino[4], Cecilia Alvarez [1,2]*

[1]Centro de Investigación en Bioquímica Clínica e Inmunología (CIBICI), Facultad de Ciencias Químicas, Universidad Nacional de Córdoba, Ciudad Universitaria, Córdoba, Argentina;

[2]Consejo Nacional de Investigaciones Científicas y Técnicas (CONICET), Argentina;

[3]Centro de Investigación en Medicina Traslacional "Severo R. Amuchástegui" (CIMETSA), Instituto Universitario de Ciencias Biomédicas de Córdoba, Córdoba, Argentina;

[4]Division of Neuroscience and Cellular Structure, Eunice Kennedy Shriver National Institute of Child Health and Human Development, National Institutes of Health, Bethesda, MD, USA;

[5]Bioinformatics and Scientific Programming Core, Eunice Kennedy Shriver National Institute of Child Health and Human Development, National Institutes of Health, Bethesda, MD USA;

[6]Molecular Genomics Core, Eunice Kennedy Shriver National Instituteof Child Health and Human Development, National Institutes of Health, Bethesda, MD, USA.

[7]Instituto de Investigación Médica Mercedes y Martín Ferreyra INIMEC-CONICET-UNC, Córdoba, Argentina;

*Corresponding authors.

Abstract

The transition from a neural progenitor to a mature, polarized neuron requires a substantial and strictly coordinated investment of cellular energy. While the genetic cascades governing cytoskeletal remodeling and structural polarity are well documented, how these programs are metabolically supported during early differentiation remains a fundamental question in neurobiology. In this study, using three different species as study models: rats, mice, and humans and an unbiased transcriptomic approach, we identify the transcription factor CREB3L1 as a key molecular regulator that dynamically modulates both neuronal morphogenesis and cellular bioenergetics. Through targeted CRISPR-Cas9 knockout in human iPSC-derived glutamatergic neurons and functional silencing in rodent models, we demonstrate that the loss of CREB3L1 disrupts critical cytoskeletal networks required for axonogenesis. This structural collapse is accompanied by a bioenergetic paradox: CREB3L1-deficient neurons trigger a compensatory upregulation of mitochondrial biogenesis programs; however, these upregulated networks are functionally defective, exhibiting dissipation of membrane potential and impaired metabolic capacity. *In vivo* assays using *in utero* electroporation reveal that this bioenergetic failure delay developing neurons in a multipolar state, thereby impairing the multipolar-to-bipolar transition relevant for proper cortical integration. Collectively, our findings define CREB3L1 as a transcriptional regulator controlling both structural architecture and mitochondrial homeostasis, offering a novel, cross-species framework for understanding neurodevelopmental vulnerabilities and neuropathologies.

Keywords: CREB3L1, transcription factor, neurons, neuronal differentiation, gene regulation, i3Neurons, mitochondrial function.

Introduction

Neural development is a highly regulated process. Beyond the initial proliferation of neural stem cells, the progression toward mature, functionally integrated circuits requires coordinated neural induction, progenitor specification, and terminal differentiation. This progression is governed by a transcriptional architecture in which networks of basic helix-loop-helix (bHLH) factors, such as Neurogenins and NeuroDs, cooperate with homeobox genes (e.g., the Hox family, Tbr1) and region-specific regulators, such as Pax6 and Sox2, to orchestrate transcriptional programs underlying cell-fate specification and neuronal differentiation[1–4]. These factors integrate a constant stream of extrinsic signals—including Notch, Wnt, FGF, and Sonic Hedgehog—to activate the genetic programs required for neuronal migration and circuit formation[5,6]. Disruptions within this regulatory framework are frequently linked to neurodevelopmental disorders.

The execution of these genetic programs is intimately linked to cellular bioenergetics. Emerging evidence suggests that the transition from a multipotent progenitor to a committed neuron requires metabolic reprogramming, shifting from glycolysis to oxidative phosphorylation (OXPHOS)[7,8]. In this developmental context, mitochondria function not only as sources of ATP, but also as dynamic metabolic hubs that modulate calcium signaling, reactive oxygen species (ROS) homeostasis, and the synthesis of precursors essential for biomass expansion[9–11]. Consequently, the coordination of mitochondrial biogenesis, mitochondrial fission/fusion dynamics, and quality control mechanisms—such as mitophagy—is essential to meet the localized energy demands of growing neurites [12,13].

The structural hallmark of neuronal maturation is the acquisition of a polarized phenotype, characterized by the emergence of distinct axonal and dendritic compartments[14–17]. Maintaining this complex shape demands a massive amount of energy to keep the cell connected to the rest of the system[18,19]. Specifically, axonal specification and the critical multipolar-to-bipolar transition are highly dependent on the positioning and metabolic efficiency of the mitochondria[20,21]. Inadequate bioenergetic support often manifests as impaired neurite outgrowth and persistent defects in neuronal architecture[22,23].

Members of the CREB3 family of transcription factors—composed of CREB3 and CREB3L1 through CREB3L4—have gained attention as regulators of tissue-specific secretory and metabolic programs. CREBs are synthesized as endoplasmic reticulum (ER)–anchored transmembrane proteins that traffic to the Golgi apparatus, where they undergo regulated intramembrane proteolysis. This processing releases an N-terminal fragment that translocates to the nucleus to regulate gene expression[24,25]. Within the central nervous system, family members exhibit specialized roles: CREB3 is involved in Golgi apparatus maintenance in hippocampal neurons, while CREB3L2 has been implicated in oligodendrocyte maturation and cell differentiation[26–28]. Emerging evidence has linked CREB3L1 (also known as OASIS)[29], to astrocyte differentiation and neuroendocrine regulation within the mature hypothalamus[30,31]. In magnocellular neurons, CREB3L1 acts as a critical endoplasmic reticulum stress sensor that maintains proteostasis via the PERK pathway and directly modulates the transcriptional programs of neuropeptides and hormone-processing enzymes under physiological stress[32]. Moreover, we previously demonstrated that CREB3L1 is essential for the structural adaptation of the secretory pathway in response to high biosynthetic demand[33,34]. However, despite these insights into specialized

neuroendocrine circuits and mature cell types, the specific contribution of CREB3L1 to early neurodevelopment and neuronal maturation remains largely uncharacterized. This gap in our understanding underscores the need for an unbiased approach to map the downstream molecular networks governed by CREB3L1 during neuronal morphogenesis.

In the present study, we combined transcriptomic and functional approaches to define the role of CREB3L1 during early neuronal maturation. By employing gene silencing in murine models and targeted CRISPR-Cas9 deletion in human iPSC-derived glutamatergic neurons (i3Neurons), we demonstrate that CREB3L1 regulates the structural and metabolic programs indispensable for neuronal morphogenesis. Our RNA-sequencing data reveal that CREB3L1 deficiency disrupts genes associated with specialized cytoskeletal networks—including mitotic machinery repurposed for axonogenesis—while simultaneously disrupting the transcriptional programs that maintain mitochondrial homeostasis. These findings identify CREB3L1 as a novel factor concurrently regulating the transcriptional networks underlying cytoskeletal dynamics and cellular bioenergetics, providing new insights into the mechanisms underlying the multipolar-to-bipolar transition and its potential relevance in neuropathological contexts.

RESULTS

The loss of CREB3L1 triggers a transcriptomic remodeling of neuronal and metabolic programs.

To dissect the transcriptional regulatory network governed by CREB3L1 during the earliest stages of human neurodevelopment, we employed a synchronized differentiation model. We used human induced pluripotent stem cells (iPSCs) engineered to express the pro-neuronal

transcription factor Neurogenin 2 (NGN2) under the control of a doxycycline-inducible promoter[35,36]. Upon addition of doxycycline, these cells rapidly and efficiently transition into a largely homogeneous population of glutamatergic cortical-lineage neurons, hereafter referred to as i3Neurons (Fig. 1A). To investigate the specific contribution of CREB3L1, we generated knockout (KO) iPSC lines using CRISPR-Cas9-mediated gene editing. Molecular characterization of the edited clones identified a 9-base-pair deletion in CREB3L1 exon 1 (Fig. 1B). The impact of the mutation on protein expression was confirmed via SDS-PAGE and immunoblot analysis, which demonstrated a loss of detectable CREB3L1 protein in differentiated i3Neurons (Fig. 1C).

We then performed unbiased RNA sequencing (RNA-seq) on four independent replicates of WT and CREB3L1_KO i3Neurons at 7 days in vitro (DIV7), a critical window for initial neurite outgrowth and specification. Across our samples, we detected 37.599 genes with nonzero expression. Differential expression analysis identified 700 genes significantly upregulated and 657 genes significantly downregulated (padj < 0.05, $|\log2FC| > 1$) in CREB3L1_KO compared to WT i3Neurons (Fig. 1D). Principal Component Analysis (PCA) of variance-stabilized counts showed clear separation between WT and CREB3L1_KO genotypes (Fig. 1E). A heatmap of the top 100 DEGs by adjusted p-value illustrates the consistent expression pattern across biological replicates (Fig. S1A). To extract biological meaning from these gene changes, we first performed Gene Set Enrichment Analysis (GSEA) using the Gene Ontology (GO) database across Biological Process (BP), Cellular Component (CC), and Molecular Function (MF) domains (Fig. 1F–K). Among the downregulated genes in CREB3L1_KO i3Neurons, GO BP analysis revealed a significant suppression of cell cycle and mitotic networks (e.g., sister chromatid segregation, mitotic nuclear division,

chromosome separation), alongside processes indispensable for structural differentiation, such as axonogenesis, axon guidance, axon development, and neuron projection guidance (Fig. 1F). Since terminally differentiated i3Neurons are post-mitotic, the downregulation of mitotic components—such as specific kinesins and microtubule regulators—aligns with the concept that developing neurons repurpose mitotic machinery to generate mechanical sliding forces for axonal extension[37–39]. Consistent with the downregulation of genes involved in mitotic machinery and microtubule dynamics, GO CC enrichment showed a marked depletion of cellular structures associated with chromosome organization and microtubule-based architecture, including the kinetochore, condensed chromosome, spindle, microtubule, and axoneme (Fig. 1H). At the molecular function level, GO analysis identified reduced enrichment of functions related to neuronal signaling and cytoskeletal regulation, including transmembrane-ephrin receptor activity, glutamate receptor activity, and tubulin binding, as well as DNA-binding transcription factor activity (Fig. 1J). Inspecting the individual genes within these terms, we found the microtubule-stabilizing protein *MAPT* (Tau) and the centrosomal adapter *TACC3* which are essential for maintaining microtubule bundle integrity and steering within the axonal shaft [37,40]. In addition, mitotic kinesins such as *KIF11* (Eg5), *KIF18B*, and *KIFC1* (HSET)—which typically govern spindle bipolarity and chromosome sliding in dividing cells—are repurposed in post-mitotic neurons to regulate microtubule-microtubule sliding forces, a mechanical process strictly required for growth cone turning and axon collateral branching, and these were downregulated upon CREB3L1_KO (Fig. S1B) [38,39,41]. Together, these transcriptomic changes lead us to hypothesize that CREB3L1 deficiency may impair the specialized cytoskeletal motor network, including the repurposed mitotic machinery , thereby potentially compromising axonogenesis, a process indispensable for early morphological differentiation.

Conversely, upregulated genes in CREB3L1_KO neurons showed a strong enrichment for aerobic bioenergetics and mitochondrial processes. Top enriched GO BP terms included aerobic respiration and respiratory electron transport, complex I biogenesis, complex IV assembly, mitochondrial translation, and mitochondrial protein import (Fig. 1G). Consistent with these mitochondrial processes, GO CC analysis highlighted enrichment of terms associated with mitochondrial structure and organization, including mitochondrial protein-containing complex, respirasome, mitochondrial inner membrane, and mitochondrial matrix (Fig. 1I). Likewise, GO MF analysis showed significant upregulation of respiratory and metabolic activities, including NADH dehydrogenase activity, electron transfer activity, oxidoreduction-driven active transmembrane transporter activity, and proton channel activity (Fig. 1K).

To gain deeper mechanistic insight into these transcriptomic changes, we performed GSEA mapping against the REACTOME pathway database (Fig. 2A-B). Downregulated pathways in CREB3L1_KO condition were predominantly linked to cell cycle progression and neuronal projection/guidance mechanisms (Fig. 2A). In contrast, the upregulated gene set showed a robust enrichment of mitochondrial and bioenergetic pathways, including aerobic respiration, respiratory electron transport, complex I biogenesis, complex IV assembly, mitochondrial protein import, and mitochondrial translation, as well as pathways related to metabolism and fatty acid metabolism (Fig. 2B). Together, these findings further support a shift from neuronal signaling and structural functions toward enhanced mitochondrial and metabolic programs following CREB3L1 loss.To examine the individual genes associated with the selected enriched terms, we focused on the GO BP terms highlighted in red in Fig. 1F–G and displayed the expression patterns of selected DEGs associated with these terms

(Fig. 2C-D). We selected 50 genes—based on the highest degree of overlap and greatest differential expression (padj)— associated with the four downregulated GO terms shown in Fig. 1F: neuron projection guidance, axon guidance, axon development, and axonogenesis. These genes were grouped into four functional categories to highlight their biological roles during axon growth. Among these genes with reduced expression (Fig. 2C), we observed a coordinated decrease in key structural and regulatory factors across these four functional blocks: axonal guidance (e.g., *SEMA3A, SEMA3E, ROBO1/2, PLXNA4*), morphogenesis/cytoskeleton (e.g., *MAPT, GAP43, TUBB3, DCX*), cell fate (e.g., *PAX6, GBX2, GLI3, EGR2*), and signaling and synapses (e.g., *TIAM1, RELN, BDNF, GDNF*). These genes are essential for microtubule stabilization and growth cone dynamics.

To further investigate the metabolic adaptations associated with CREB3L1 deficiency, we the four most significantly enriched upregulated GO terms highlighted in red in Fig. 1G aerobic respiration and respiratory electron transport, Respiratory electron transport, complex I biogenesis and mitochondrial protein degradation (Fig. 2D). A subset of the 50 most strongly up-regulated genes associated with these terms was selected and stratified into four functional groups to resolve their potential contributions to mitochondrial metabolism (Fig. 2D). CREB3L1-deficient neurons exhibited a robust upregulation of these genes critical for aerobic energy production. Notably, key genes across these four metabolic categories were significantly upregulated, including those involved in respiratory chain entry (complexes I and II; e.g., *ND2/4/5, NDUFS1-3, SDHA/B/C*), oxidative phosphorylation/ATP production (complexes IV and V, as well as complex V ATP synthase; e.g., *COX2, ATP5/8, ATP5F1A/B/C*), transport and structure (e.g., *TOMM20, MFN2, SLC25A12/13/18*), and metabolism and signaling/stress sensors (e.g., *TGFB1, PPARGC1A, PRKAG2, PPARA*).

Collectively, these findings reveal a transcriptional shift in CREB3L1-deficient neurons: a suppression of the cytoskeletal and axon guidance programs required for structural maturation, paired with an upregulation of mitochondrial and bioenergetic pathways. This pattern suggests that structural and metabolic programs are co-regulated during neuronal differentiation.

CREB3L1 expression and its link to mitochondrial homeostasis are conserved in primary hippocampal neurons

While i3Neurons provide a powerful human genetic background and scalability [42], primary hippocampal cultures remain the gold standard for dissecting the discrete stages of neuronal polarization and morphogenesis. Thus, to validate our findings in a well-established model of neuronal morphogenesis, we examined the role of CREB3L1 in primary rat hippocampal neurons. In this system, differentiation is characterized by a predictable sequence of structural steps starting with symmetric, newly plated cells (defined as stage 1) followed by the extension of multiple identical minor neurites (stage 2). At this point, cellular symmetry is broken when a single neurite undergoes accelerated growth to become the axon (stage 3), while the remaining processes mature into dendrites (stage 4 and 5). This classic model allows us to visualize exactly how and when metabolic or genetic changes disrupt the architectural timeline of a developing neuron [43,44].

We first characterized the expression of CREB3L1 during neuron differentiation. Immunofluorescence microscopy together with SDS-PAGE and immunoblot analysis revealed that CREB3L1 expression significantly increases as neurons mature, showing a 2-fold increase from DIV1 to DIV7 (Fig. 3A-D). To investigate the effects of CREB3L1 loss in this model, we generated lentiviral particles carrying two independent shRNA sequences

targeting *Creb3l1*. Immunoblotting confirmed that both sequences reduced CREB3L1 protein levels by approximately 40% (#1) and 60% (#2) compared to scrambled controls (Fig. 3F-G).

Using this validated gene silencing model, we sought to determine whether the transcriptomic alterations observed in the CREB3L1-KO i3Neurons were conserved in these primary cells. Hippocampal neurons were transduced at DIV0 and processed at DIV3 (as outlined schematically in Fig. 3E). We focused on candidate genes with the significant changes observed in the CREB3L1_KO i3Neurons, particularly those strongly implicated in mitochondrial function. We report that silencing CREB3L1 resulted in significant upregulation of the same mitochondrial markers, specifically *PPARGC1A* (PGC1α), the master regulator of mitochondrial biogenesis[45], *MFN2* (MTFN-2), a key GTPase involved in outer membrane fusion and organelle anchoring[46], and *TOMM20*, a marker for mitochondrial outer membrane mass[47] (Fig. 3H-J). At the protein level, SDS-PAGE and immunoblot confirmed the increased levels of PGC-1α, MFN2, and TOMM20 in shCREB3L1 neurons (Fig. 3K-N). These findings suggest that the link between CREB33L1 deficiency and mitochondrial upregulation is a consistent, cross-species phenomenon relevant to understanding neuronal metabolic homeostasis.

CREB3L1 deficiency drives an accumulation of dysfunctional mitochondria

Having established that CREB3L1 silencing leads to upregulation of mitochondrial markers, we next investigated whether mitochondrial morphology and function were altered in shCREB3L1 hippocampal neurons. To directly visualize mitochondria, neurons were labeled with MitoTracker[48] and analyzed using a grayscale images. In addition to the panel, we show a representation of fluorescence intensity based on a thermal pseudocolor (LUT) (Fig. 4A).

Quantitative analysis revealed that shCREB3L1 neurons exhibited significantly higher intensity levels and increased mitochondrial area relative to soma compared to control neurons (Fig. 4B-C). This increase was not attributable to differences in cell size, as the soma area was comparable between control and shCREB3L1 neurons, indicating a greater proportion of the soma occupied by mitochondria. This mitochondria expansion was further confirmed by confocal Z-stacking and 3D rendering (Airyscan), which revealed a denser, more interconnected mitochondrial morphology in shCREB3L1 cells (Fig. 4D).

We next asked whether the observed increase in mitochondrial mass reflected a genuine functional enhancement or a compensatory response to underlying mitochondrial dysfunction. To explore these possibilities, we revisited our transcriptomic data. Within the downregulated set in the CREB3L1-KO i3Neurons, we identified a subset of mitochondrial-related terms pointing to an imbalance in mitochondrial dynamics and bioenergetic maintenance. Gene set enrichment analysis revealed an enrichment of terms such as mitochondrial fission (GO:0034643), mitochondrion morphogenesis (GO:0070584), and regulation of membrane potential (GO:0042391) (Fig. 4E). Network analysis of core enrichment genes within these categories pointed to potential nodes of interest. Specifically, downregulation of *OPA1*, a master regulator of mitochondrial inner-membrane fusion[49], and the fission component *MIEF2* (MiD49)[50], provides intriguing transcriptomic clues that may align with the expanded mitochondria observed in our 3D Airyscan imaging. In parallel transcriptional modulation of *MAPT*, a known regulator of microtubule-based axonal transport and mitochondrial network architecture[51], hints at potential alterations in organelle trafficking and morphology (Fig. 4E). Furthermore, we observed reduction in genes involved in regulating membrane potential, including the voltage-gated potassium channel subunits

KCNK9 and *KCNK10*[52], and the non-muscle myosin motor *MYH14*, which is involved in mechanical organelle remodeling and mitochondrial genome distribution[53] (Fig. 4E). Given that the ion channels affect the electrochemical gradient across the inner mitochondrial membrane, we set out to analyze this phenomenon in greater detail and determine whether it causes a functional bioenergetic defect. To test this, we monitored mitochondrial membrane potential ($\Delta\Psi m$) in primary hippocampal neurons infected with lentiviruses carrying shRNAs and incubated with the voltage-sensitive fluorophore TMRE[54] (Fig. 4F-H). As a positive control for depolarization, the uncoupler CCCP was utilized, which induced a sharp reduction in fluorescence intensity (Fig. 4F and H). Interestingly, despite their greater mitochondrial mass, shCREB3L1 neurons (identified by GFP expression) showed a significant decrease in TMRE signal compared to control neurons (Fig. 4F-H). This indicates that the expanded mitochondrial networks observed in of CREB3L1-depleted cells have attenuated membrane potential. This combination of increased organelle mass and reduced polarization suggests an underlying homeostatic imbalance. Therefore, rather than reflecting enhanced metabolic capacity, this expanded mitochondria likely results from a stress-induced compensatory fusion mechanism, consistent with the reduced $\Delta\Psi m$ and suggestive of impaired clearance or altered distribution of dysfunctional mitochondria. Collectively, these findings suggest that CREB3L1 plays a role in maintaining the balance between mitochondrial structural homeostasis and functional competence. In its absence, neurons undergo a compensatory yet inefficient expansion of the mitochondrial network but fail to maintain their bioenergetic competence.

CREB3L1 pathways regulate axonal specification and the multipolar-to-bipolar transition

Based on the observation that CREB3L1-deficient neurons accumulate an expanded, yet hypo polarized mitochondrial network, we investigated whether this bioenergetic discordance affected neuronal morphogenesis. The downregulation of genes related to axonal development in our transcriptomic data (Figs. 1–2) suggested a failure in neuronal growth and maturation programs; this is consistent with a scenario in which insufficient mitochondrial function, despite increased mass, fails to meet the energy demands of axonal specification. Parallelly, given that CREB3L1 may also modulate structural components independent of mitochondrial bioenergetics, we next examined molecular effectors of the cytoskeleton.

In our RNA-seq data, we find the downregulation of certain of the genes associated with axonal development and neuronal projection guidance to be of interest (Fig. 2C). Specifically, we observed the loss of *MAPT* (encoding Tau, the primary microtubule-stabilizing protein in axons)[15], *GAP43* (crucial for growth cone plasticity and regeneration)[55], *TIAM1* (a GEF for Rac1 that orchestrates the actin dynamics necessary for neurite elongation)[56] alongside with key markers of neuronal maturity and structure such as *TUBB3* (beta-3 tubulin)[57] and *DCX* (Doublecortin)[58]

In CREB3L1-silenced primary hippocampal neurons, quantitative RT-PCR confirmed significant downregulation of *MAPT*, *DCX, GAP43*, *TUBB3* and *TIAM1* consistent with the i3Neurons KO data (Fig. 5A-E), whereas *MAP2*[59] mRNA levels were increased (Fig. 5-F). A comparative heatmap integrating the i3Neurons knockout (i3N KO) and the rat neurons knockdown (RN KD) datasets revealed a similar pattern of gene expression changes, indicating that the transcriptional effects of CREB3L1 loss are conserved across models (Fig. 5G).

Subsequently, we investigated how the downregulation of these regulators of axonal identity, together with the metabolic imbalance, impacts overall neuronal development. To enable direct visualization and quantitative analysis of cellular morphogenesis in CREB3L1-depleted cells, we employed a GFP-based expression system (this system also ensures consistency with subsequent *in utero* electroporation experiments). Using the shCREB3L1#1 sequence cloned into a pCAGIGFP vector, we confirmed a ~40% reduction in CREB3L1 by immunofluorescence microscopy in transfected hippocampal neurons (Fig. S2A and B). We report that depletion of CREB3L1 resulted in inhibition of total neurite growth and axonal length in 3DIV neurons (Fig. 5H–K). In contrast, CREB3L1 overexpression using a pTracer-WT-GFP vector (resulting in an approximate twofold increase in CREB3L1 levels**;** Fig. S2C and D) led to increased axonal and total neurite growth relative to control cells (Fig. 5L–O).

To determine whether axonal identity remained intact despite the observed morphological defects, we stained neurons at 3 DIV for Tau-1, a well-established marker of axonal identity[15,60,61]. At this stage of development (stage 3), distal enrichment of dephosphorylated Tau is widely used as an indicator of successful axonal specification and microtubule stabilization[62]. In CREB3L1-depleted cells, approximately 50% of neurons showed a decreased distal Tau-1 enrichment in the axon (red arrow, Fig. 5P), indicating impaired axonal specification (Fig. 5P and R). Conversely, CREB3L1 overexpression preserved the distal Tau-1 pattern (Fig. 5Q and S; white arrows).

During cortical development, nascent neurons initially adopt a multipolar morphology in the intermediate zone before undergoing a critical transition from multipolar to bipolar. This morphological change, which requires precise polarization and axonal specification, is essential for proper migration toward the cortical plate[63,64]. To determine whether CREB3L1

346 regulated structural and bioenergetic functions are compromised within the complex
347 architecture of the developing brain, we performed *in utero* CREB3L1 depletion by
348 electroporation on E15.5 mouse embryos, targeting progenitor cells in the ventricular zone
349 (Fig. 6A). This approach allows for the analysis of neuronal migration and morphological
350 transition in the developing neocortex at stage E18.5 (Fig. 6B) [63,65].

351 Initially, we examined radial migration by analyzing the distribution of GFP-positive cells
352 across the cortical layers: Ventricular/Subventricular Zone (VZ/SVZ), Intermediate Zone
353 (IZ), and Cortical Plate (CP). Interestingly, the percentage of neurons entering the CP was
354 comparable between shScrambled and shCREB3L1 treatments, suggesting that CREB3L1 is
355 not required for the initiation or progression of radial migration per se (Fig. 6C). However,
356 high-resolution morphological analysis within the cortical architecture revealed defects in
357 neuronal polarization. Quantification of neuronal morphology across all cortical layers
358 showed that, while control neurons (shScrambled) exhibited a 75/25 multipolar/bipolar ratio,
359 shCREB3L1 neurons displayed an 86/14 ratio (Fig. 6D). Consistent with this, control
360 neurons displayed a classic bipolar morphology—characterized by a single, vertically
361 oriented leading process essential for proper orientation within the IZ and CP layers (Fig. 6E,
362 red arrows, and 6F)—whereas a higher proportion of shCREB3L1 neurons remained
363 multipolar or rounded in those layers (Fig. 6E, blue arrows, and 6F), lacking a clearly defined
364 leading process. Quantitative analysis confirmed a significant increase in multipolar
365 morphologies in both the IZ and CP of CREB3L1-depleted brains (Fig. 6F). Together, these
366 *in vivo* findings demonstrate that CREB3L1 is a critical regulator of the multipolar-to-bipolar
367 transition in the developing neocortex. In its absence, some of the neurons undergo a
368 developmental delay at the multipolar stage, limiting their ability to establish the structural

polarization necessary for proper orientation and mature cortical integration. This final piece of evidence corroborates our transcriptomic and *in vitro* data, establishing CREB3L1 as a key regulator of neuronal structural integrity during brain development.

Discussion

Our study identifies CREB3L1 as a pivotal transcriptional node that couples structural programs required for neuronal polarization and maturation with mitochondrial bioenergetics. By integrating transcriptomic profiling in human i3Neurons with functional validation in primary cultures of rat hippocampal neurons and *in vivo* mouse models, we provide a cross-species framework demonstrating that CREB3L1 plays a key role in the multipolar-to-bipolar transition and axonal specification. Furthermore, our findings uncover a previously unrecognized role for CREB3L1 in the regulation of mitochondrial biogenesis and functional competence, positioning this transcription factor as a central factor controlling energy metabolism and neuronal development.

CREB3L1 controls neuronal-specific genetic programs.

The RNA sequencing analyses in human CREB3L1-KO i3Neurons revealed substantial downregulation of genes associated with neuronal development and maturation, including *DCX, MAPT, TIAM1, GAP43, TUBB3,* and *MAP2*, reflecting a broad pattern disruption of neuronal identity programs. Validation in rat hippocampal neurons confirmed that loss of CREB3L1 reduces the expression of key developmental and maturation markers, supporting a conserved role for CREB3L1 in shaping neuronal gene expression programs across species. The enrichment of axonogenesis and neuron-specific terms among CREB3L1-regulated transcripts is consistent with a role for CREB3L1 in promoting neuronal development, rather

than acting as a general regulator of cell fate. Intriguingly, our transcriptomic analysis also revealed a significant suppression of cell cycle and mitotic programs upon CREB3L1 loss. While CREB3L1 is recognized as a potent cell-cycle inhibitor and tumor suppressor[26,66], its deficiency in post-mitotic neurons resulted in the downregulation—rather than upregulation—of division-related networks. This paradox strongly aligns with an emerging neurodevelopmental paradigm where post-mitotic neurons actively repurpose canonical mitotic machinery (such as specific kinesins and kinetochore components) to modulate microtubule sliding and generate the mechanical forces necessary for growth cone navigation[67]. Therefore, the synchronized downregulation of cell division and axonogenesis genes indicate that CREB3L1 orchestrates a specialized, co-opted cytoskeletal program indispensable for early axonal outgrowth.

Functional assays demonstrate that CREB3L1 depletion reduces total neurite length and axonal growth in developing hippocampal neurons, while CREB3L1 overexpression enhances growth, with a more pronounced effect on axons. These effects on neurite dynamics, along with altered Tau-1 localization in distal axons, indicate that CREB3L1 influences axon specification and cytoskeleton organization. This role is reminiscent of other CREB3 family members; for instance, CREB3L2 has been shown to modulate neurite outgrowth in PC12 cells[28], while CREB3 (Luman) is involved in regulation of the intrinsic elongating form of sensory axon regeneration and in Golgi apparatus organization a prerequisite for polarized growth[27,68].

The observation that CREB3L1 deficiency induces a persistent multipolar state without significantly impairing radial migration itself suggests a highly specific role in the multipolar-bipolar transition. This transition constitutes a well-characterized developmental

checkpoint, where neurons must break symmetry to exit the Intermediate Zone (IZ) and enter the Cortical Plate (CP)[64,69]. In this context, our results contrast with the phenotypes observed in classic migration mutants, such as Lis1[70], where neurons exhibit impaired nucleokinesis (nuclear movement) and terminal arrest during radial locomotion, or Dcx, where neurons often fail to reach their lamellar target[71]. In CREB3L1-deficient neurons, nucleokinesis does not appear to be altered , whereas morphological maturation is disrupted. This phenotype resembles conditions in which coordination between the microtubule-organizing center (MTOC) and the leading process is impaired [72,73].

Since CREB3L1 regulates *MAPT* (Tau) and *TUBB3*, its absence likely compromises the stabilization of a single dominant main neurite, resulting in persistence of multipolar morphology characterized by transient extension and retraction of multiple processes[74]. This arrest can be further explained by decreased expression of *TIAM1* and *GAP43* in both CREB3L1-KO i3Neurons and shCREB3L1 treated neurons. TIAM1 protein is a Rac1 GEF that coordinates actin-microtubule crosstalk required for neurite stabilization during bipolar transition [56,75]. Reduced TIAM1 levels, may impair the selection of a dominant axon. Furthermore, the loss of Tau (*MAPT*) expression compromises the structural rigidity of the newly formed bipolar axis[76].

During the multipolar-to-bipolar transition, neurons undergo profound cytoskeletal reorganization, in which selective microtubule stabilization, mediated by MAPs and specific tubulin isoforms, provides a scaffold to support metabolic demands of elongation[16,77]. Disruption of this scaffold may impair efficient transport and contribute to the persistence of multipolar morphology[78]. Together, these findings suggest that CREB3L1supports neuronal

morphogenesis by coordinating transcriptional programs required for cytoskeletal organization and axonal growth.

CREB3L1 links regulation of the secretory pathway with mitochondrial function.

The discovery that CREB3L1, a well-known ER stress transducer[79,80], modulates mitochondrial gene networks establishes a new connection between the secretory pathway and neuronal bioenergetics. Traditionally, the CREB3 family has been characterized by its role in expanding the capacity of the ER and Golgi apparatus to meet high biosynthetic demands[33,81]. Our data suggest for the first time that CREB3L1 activity is also important for maintaining mitochondrial function during neuronal differentiation.

The observed upregulation of mitochondrial biogenesis factors (*PGC-1α, MFN2*) alongside a dissipated membrane potential suggests a compensatory mitochondrial response to bioenergetic stress[82,83]. In this scenario, CREB3L1-deficient neurons may sense a bioenergetic imbalance, triggering transcriptional programs that expand mitochondrial content. However, this response fails to restore functional membrane potential, as evidenced by reduced TMRE signal, and may contribute to the failure of energy-demanding processes such as axonal specification.

This uncoupling between mass and function suggests that CREB3L1 may act beyond simply regulating mitochondrial abundance, potentially contributing to mitochondrial quality control. Without CREB3L1, the neuron may be unable to maintain the structural integrity of the electron transport chain or the electrochemical gradient necessary for OXPHOS, leading to the accumulation of dysfunctional mitochondria[13].

As neurons transition from progenitor to polarized cells, the demand for membrane synthesis and protein trafficking increases substantially. Previous work from our group identified CREB3L1 as a regulator of the secretory pathway [34]; the current findings extend this role by suggesting that CREB3L1 may coordinate biosynthetic demand with mitochondrial function. This coordination may involve direct communication between the ER and mitochondria, potentially through contact sites (MAMs), which regulate calcium and lipid exchange required for mitochondrial activity[84,85]. Notably, the dysregulation of OPA1 and voltage-gated calcium channel subunits observed in our transcriptomic data is consistent with disrupted ER-mitochondria communication. OPA1 is not only a fusion protein but also a critical regulator of MAMs, which modulate calcium transfer and lipid metabolism[86,87]. In this context, the persistence of a multipolar-to-bipolar state in CREB3L1-deficient neurons can be interpreted as a consequence of insufficient bioenergetic support for neuronal polarization. Together, these findings point to a potential link between CREB3L1 and secretory and metabolic aspects relevant to neuronal maturation.

Implications in neurodevelopmental and neurodegenerative contexts

While it is well established that homozygous loss-of-function mutations in the CREB3L1 gene cause osteogenesis imperfecta (OI) type XVI, severe skeletal dysplasia characterized by defective collagen secretion[88] , its physiological relevance to proper neuronal growth has largely gone unnoticed, overshadowed by its pronounced skeletal phenotype. Our findings expand this pathological landscape by revealing that CREB3L1 is also important for mitochondrial bioenergetics and cytoskeletal dynamics during neuronal development. Given that correct cortical connectivity relies heavily on the precise timing of differentiation and energy supply, CREB3L1 alterations could contribute to neurodevelopmental disorders

characterized by impaired structural connectivity; this offers a new framework for investigating previously undetected neurological comorbidities in patients carrying these genetic variants. Furthermore, the striking link between CREB3L1 deficiency and defective mitochondrial networks suggests a broader vulnerability to neurodegenerative processes where metabolic failure and secretory stress converge, a notion strongly supported by our KEGG pathway analysis, which revealed a distinct enrichment of pathways associated with neurodegenerative diseases. Ultimately, these observations underscore the need for future research to identify CREB3L1 targets in both neuronal and glial compartments and to elucidate its precise regulatory interplay with ER-Golgi stress pathways in the CNS.

Concluding remarks

Overall, our results support the emerging view that neurodevelopment is regulated by both metabolic and transcriptional processes[89]. By influencing both cytoskeletal dynamics and ER-related secretory programs alongside mitochondrial function, CREB3L1 acts as a regulatory factor that supports bioenergetic homeostasis in developing neurons. In its absence, an imbalance emerges in which mitochondrial biogenesis is increased, yet functional output remains compromised, resulting in a developmental decoupling between metabolic capacity and structural demand. This imbalance is associated with the structural maturation defects observed in our model, highlighting a broad role for CREB3L1 in parallel metabolic and transcriptional programs during neuronal development.

Materials and Methods

Human iPSC culture and neuronal differentiation

Human iPSCs expressing doxycycline-inducible NGN2 (neurogenin) [35,36] were cultured on Matrigel-coated dishes in Essential 8 Flex Medium (E8Flex) (Thermo Fisher Scientific) according to the manufacturer's instructions. In brief, cells were passaged with Accutase (STEMCELL Technologies) when 70% confluent and then seeded into E8Flex supplemented with 10 μM Y-27632 dihydrochloride, a ROCK inhibitor (S1049, Selleck Chemicals). After 24 hours, the medium was replaced with E8Flex without ROCK inhibitor and maintained until the following passage. Differentiation of iPSCs to i3Neurons was performed as described Wang C et al. Stem Cell Reports. 2017; Fernandopulle MS et al. Curr. Protoc. Cell Biol. 2018. iPSCs were seeded on day 0 in induction medium containing DMEM/F12 (11330032, Gibco, Thermo Fisher Scientific) with 1× non-essential amino acids (NEAAs) (11140050, Gibco, Thermo Fisher Scientific), 1× GlutaMAX (35050061, Gibco, Thermo Fisher Scientific), 1× N2A supplement (17502048, Gibco, Thermo Fisher Scientific), 2 μg ml−1 doxycycline (D9891, MilliporeSigma), and 10 μM Y-27632 dihydrochloride ROCK inhibitor (S1049, Selleck Chemicals). The induction medium was changed daily for 3 days. Cells were then lifted with Accutase, counted, and plated in neuronal culture medium consisting of BrainPhys medium (5790, STEMCELL Technologies) supplemented with 10 ng ml−1 neurotrophin-3 (450-03, PeproTech, Thermo Fisher Scientific), 10 ng ml−1 BDNF (450-02, PeproTech, Thermo Fisher Scientific), 1× B-27 supplement serum-free (17504044, Gibco, Thermo Fisher Scientific), 2 μg ml−1 doxycycline (D9891, MilliporeSigma), and 1 μg ml−1 mouse laminin (23017015, Gibco, Thermo Fisher Scientific). The coverslips for growth of i3Neurons were pre-treated with poly-l-lysine

hydrobromide (P2636, MilliporeSigma) and laminin (11243217001, Roche, MilliporeSigma). Every 3 days, half of the medium was removed, and an equal volume of fresh medium was added to maintain neuronal health.

CRISPR–Cas9 KO of CREB3L1

To inactivate the CREB3L1 gene in iPSCs, we utilized the CRISPR–Cas9 system with a single guide RNA (sgRNA) targeting each gene. For CREB3L1 KO, the sgRNA sequence was designed in Benchling (https://benchling.com) targeting the first exon. We created one forward and one reverse oligonucleotide bearing the selected sgRNA (uppercase) and the sequence necessary for cloning into the px458 plasmid (lowercase): forward 5′-caccgCTTGGGGGATCTGAACGAGT and reverse 5′-aaacACTCGTTCAGATCCCCCAAGc. The guides were separately cloned into the px458 plasmid (Addgene plasmid 48138). In brief, the px458 plasmid was cut with BbsI, and the annealed oligonucleotides were inserted using T4 DNA ligase. The insertion was verified by sequencing. The plasmids bearing the sgRNAs were co-transfected into iPSCs using Lipofectamine 2000 (Thermo Fisher Scientific). Forty-eight hours later, single cells were sorted into 96-well plates based on GFP-positive signal. The single cells were allowed to grow in complete E8Flex medium supplemented with RevitaCell (A2644501, Thermo Fisher Scientific) for 3 weeks. When colonies were visible, cells were transferred to a 24-well dish, then to a 6-well dish, and grown to confluency. Cells were then harvested, and proteins and genomic DNA were isolated. The PCR products were sequenced to verify the change from the WT sequence. Further verification was conducted by SDS-PAGE and immunoblot with an antibody against CREB3L1 (Fig. 2).

548 Primary Culture of Embryonic Hippocampal Neurons

549 Culturing hippocampal neurons from rat embryonic brains was performed according to the
550 protocol of Kaech and Banker (2006). Briefly, pregnant Wistar rats (E18.5) were sacrificed,
551 and their embryos were removed, and the hippocampus was isolated and subjected to
552 enzymatic and mechanical digestion. Neurons were plated in 24 multiwell dishes containing
553 glass coverslips previously treated with 1 mg/ml of poly-L-lysine (Sigma-Aldrich,) using
554 Dulbeco's Modified Eagles Medium (DMEM; Thermo Fisher Scientific, Massachusetts,
555 United States), supplemented with 10% horse serum (Gibco, Thermo Fisher Scientific,
556 Massachusetts, United States), for 1 h at 37 C and 5% CO2. Then, the plating medium was
557 replaced by Neurobasal supplemented with B27, Glutamax, Sodium Pyruvate, and antibiotics
558 (Pen/Strep) (Thermo Fisher Scientific, Massachusetts, United States). All of the experiments
559 were approved by the Bioethical Research Committee of CIBICI-CONICET- UNC and
560 conducted following the guidelines of the manual for animal experimentation approved by
561 the institutional animal care committee (CIBICI-National Research Council and Universidad
562 Nacional de Córdoba, Argentina), the National Department of Animal Care and Health
563 (SENASA-Argentina), and Approval to conduct the study was granted by the Animal Care
564 and Ethics Committee (CICUAL) of CIBICI-CONICET-UNC (Resolution number RD-
565 2022-711-E-UNC-DEC#FCQ). Efforts were made to minimize animal suffering and to
566 reduce the number of animals used.

567 Lentivirus generation

568 Lentivirus was produced by co-expressing the obtained plasmid with psPAX2 (Addgene,
569 12260), pMD2.G (Addgene, 12259) and pAdVAntage Vector (Promega) together with the
570 plasmid encoding the shRNA sequence: Scramble forward 5′-

CCTAAGGTTAAGTCGCCCTCGCTCGAGCGAGGGCGACTTAACCTTAGG-3′ and reverse 5′-CCTAAGGTTAAGTCGCCCTCGCTCGAGCGAGGGCGACTTAACCTTAGG-3; CREB3L1#1 forward 5′-GGGGACATCAGGGCCACTGCTCTCGAGGGGGACATCAGGGCCACTGCT-3′ and reverse 5′-GGGGACATCAGGGCCACTGCTCTCGAGGGGGACATCAGGGCCACTGCT-3; CREB3L1#2 forward 5′-GGGCCCCAACACCACCATCAACTCGAGTTGATGGTGGTGTTGGGGCCC-3′ and reverse 5′-GGGCCCCAACACCACCATCAACTCGAGTTGATGGTGGTGTTGGGGCCC-3 in HEK293T cells using Lipofectamine 3000 (Thermo Fisher Scientific) according to the manufacturer's instructions. After 72 hours, the virus-containing medium was centrifuged at 700g for 5 minutes to remove cell debris and used to infect rat neurons for an additional 72 hours. The lentivirus efficiency was analyzed by SDS-PAGE and immunoblotting using CREB3L1 as a target (Fig. S1b).

mRNA isolation and qRT-PCR analysis

Neurons were seeded in 35 mm diameter plates (500,000 cells per plate) and infected after seeding with lentiviral particles containing control shRNA or CREB3L1#1. At 3 DIV, RNA was isolated using Trizol reagent (Life Technologies, USA) according to the manufacturer's instructions. The aqueous phase was separated with chloroform, and the RNA was precipitated with isopropanol for 16–18h at -20 °C. Yield was estimated by spectrophotometry using a Nanodrop (Thermo Scientific). Subsequently, the RNA (500 ng

per sample) was converted to cDNA using a commercial kit (Inbio Highway) with Oligo(dT) as a primer (Promega). Quantitative PCR (qPCR) was performed on a QuantStudio 5 (Applied Biosystems) using a SYBR Green master mix (InBio Highway). The amounts of cDNA and primers were as specified in the kit. Primers were synthesized at Macrogen (Korea). Target genes were analyzed in technical duplicates per sample across three independent biological experiments (N=3). Changes in expression were estimated using the CT method, with shRNA-sc samples as a reference. Primer sequences (5'-3'): MAPT Fw: TCCTCGCCTCCTGTCGATTA, Rv: TGCTTCTTCAGCTTTTAAGCCA; MAP2 Fw: TTGCCTGTCTGATTCTTCAGC, Rv: ATTTCCTGACTGAATGCTTCCCA; TUBB3 Fw: CAACTATGTGGGGGACTCGG, Rv: TGGCTCTGGGCACATACTTG; GAP43 Fw: CCTGTGGGAGTCCACTTTCC, Rv: GGACTCCTCAGAACGGAACA; TIAM1 Fw: CTGGGGCCTAGACACTACCT, Rv: TTGCCGTCTGGAACAGAGTC; DCX: Fw: TCAGGTAACGACCAAGACGC, Rv: CAGGGCTTGTGGGTGTAGAG; MFN2 Fw: AGTGACGTGTTGGGTGTGAT, Rv: GTGCCGATTCAGGTCCAGAT; PPARGC1A Fw: TTGACTGGCGTCATTCAGGA, Rv: CAGGGCAGCACACTCTATGT; TOMM20 Fw: CAATCGCTGTGTGTGGACAG, Rv: TCATGTTGGTGTCTGGCTCAT Expression changes were normalized to GAPDH values.

Transfection of cDNA Coding Vectors

Constructs pTracer-GFP, pTracer-CREB3L1-WT-GFP were kindly provided by Dr. Jin Ye[90] (UT Southwestern Medical Center, United States). The target sequence of the pCAG shCREB3L1 was forward: 5'-AATGCCTACGTTAAGCTATACCTCGAGGTATAGCTTAACGTAGGCATT-3', and reverse: 5'-

AAAAAAATGCCTACGTTAAGCTATACCTCGAGGTATAGCTTAACGTAGGCATT-3'. Neurons were plated in 10% HS MEM medium for 1 h, then the medium was replaced, and they were transiently transfected with Lipofectamine 2000 (Life Technologies, CA, United States), following the manufacturer's instructions. Complexes containing pCAG-shScramble, pCAG-shCREB3L1-GFP, pTracer-GFP, pTracer-CREB3L1-WT-GFP, plus Lipofectamine 2000 were resuspended in Optimem (Thermo Fisher Scientific, Massachusetts, United States) and dissolved in Neurobasal for transfection; after 2 h, it was replaced by Neurobasal supplemented with B27, Glutamax, Sodium Pyruvate, and antibiotics (Thermo Fisher Scientific, Massachusetts, United States). Experiments were performed at 72 h (3DIV) after cDNA transfection.

Primary and secondary antibodies

The following antibodies and dilutions were used in this study: anti-CREB3L1 (1:100) (Proteintech, 11235-2-AP); anti-Tau-1 at 1:200 (sigma Aldrich, clone PC1C6); anti-GFP at 1:200 (Invitrogen MA5-15256); anti-PGC1α at 1:200 (Nows NBP1-04676); anti-MTFN2 at 1:200 (Santa Cruz, sc100560); anti-TOMM20 at 1:200 (Proteintech, 11802-10AP); anti-GAPDH at 1:200 (Santa cruz, sc365062), and anti-β-actin at 1:1000 (Abcam, ab78078). The following secondary antibodies were used: anti-mouse 680 (1:1000), anti-rabbit 800 (1:1000), and anti-rabbit 680 (1:1000) (LI-COR cat. nº 92668073, cat. nº 82632213, and cat. nº 92632212, respectively). The following secondary antibodies were used: anti-mouse 546 (1:1000) (ThermoFisher, a11010), anti-rabbit Fab Alexa Fluor 594 (1:1000) (Jackson Laboratories, 111-587-003), anti-rabbit Alexa Fluor 633 (1:1000) (ThermoFisher, a21070), anti-mouse Fab Alexa Fluor 647 (1:1000) (Jackson Laboratories, 115007185), anti-chicken 488 (1:1000) (ThermoFisher, a11039).

640 SDS-Page, immunoblot, and Protein Analysis

641 Cell processing and Western blot assays were performed as described previously (Garcia et
642 al., 2017). Immunoblots were incubated overnight at 4°C with primary antibodies.
643 Membranes were washed and then incubated with the secondary antibodies IRDye 680RD,
644 IRDye 800RD, and IRDye 800RD (0.2 mg/ml, LI-COR cat. nº 92668073, cat. nº 92632215,
645 and cat. nº 92632212, respectively). Detection and quantification of near-infrared
646 fluorescence on the membranes were performed using the Odyssey CLx Imaging System
647 (LI-COR Biosciences, Lincoln, NE, United States) with Image Studio Software. Images were
648 acquired at high resolution with automatic intensity control. For Western blot quantification,
649 the intensity of each band normalized to Tubulin, β-actin, or GAPDH (loading controls) was
650 measured, and the fold change was calculated as the ratio of the normalized values in the
651 shCREB3L1 neurons versus the shScramble neurons. Three independent experiments were
652 performed. The normalized value of the control was set as one.

653 *In utero* Electroporation (IUE) and Imaging Acquisition

654 IUEs were done following previous reports [63,65,69]. Briefly, pregnant E15.5 C57bl/6 mice
655 were anesthetized with an isoflurane/oxygen mixture (4% for induction and 2% for
656 maintenance) throughout the surgery, and Tramadol (5 mg/kg) was administered as analgesia
657 during the procedure. Embryos were exposed out of the maternal belly for local injection of
658 pCAG-GFP sh Scramble or pCAG-GFP shCREB3L1 into the lateral ventricle of the brain.
659 Fast green FCF dye (Sigma-Aldrich, F7252) was co-injected with DNAs to visualize
660 injections. The brains were electroporated using a BTX electroporator (ECM 830 Square
661 Wave Pulse generator, Fisher Scientific) (1V = 39V; pulses: 5; duration: 50 ms; intervals
662 between pulses: 950 ms) with Tweezers w/Variable Gap 2 Square Platinum Electrodes

(Nepagene, Japan, CUY647P2 2). At E18.5, embryos were sacrificed to check GFP expression in shScramble or shCREB3L1 genetic contexts. Brains expressing GFP were fixed and immersed in a 30% w/v sucrose solution for 24 h, at 4 °C. The cerebral cortex of GFP-positive brains was sliced into 50-µm cortical sections using a cryostat (Leica CM1850, Leica Biosystems). Before the imaging, tissues were permeabilized with 0.3% v/v Triton X-100-PBS solution, followed by DAPI staining (15 min at RT). Samples were mounted in Mowiol solution (Sigma-Aldrich) and imaged in a Zeiss LSM-800 confocal microscope (Zeiss, Oberkochen, Germany). Images were acquired using a 20X (NA = 0.40) air objective. Several fields were acquired (from the ventricular zone to the cortical plate).

Mitochondrial analysis

To analyze mitochondrial morphology and distribution, neurons were seeded in 0.17 mm Delta TPG Dishes and infected with the lentiviruses carrying the shscrambled or shCREB3L1 sequences. They were maintained for DIV3. Subsequently, the neurons were incubated with 100 nM Mitotracker ^{48}CMXRos for 15 min, washed, and fixed with 3.7% PFA for 10 min. Images were then acquired using a Zeiss LSM 800 inverted confocal microscope (Carl Zeiss) equipped with a ×63 Plan-Apochromat objective (NA = 1.4). The fluorescence intensity of the Mitotracker was analyzed as an indicator of mitochondrial mass. In addition, the distribution of mitochondria in the soma was analyzed, considering area occupied by MitoTracker (sum of pixels with a fluorescent signal above a specific threshold) normalized by the total area of the soma (the neuronal cell body, excluding axons and dendrites). Images of mitochondria (Fig. 4D) were obtained using an LSM 980 AiryScan 2 confocal microscope, in Z-stacking and super-resolution (SR) configuration, which improved spatial resolution by

1.4 times compared to conventional confocal microscopy (objective: 63x with oil, 1.4 NA; pinhole: 1 AU; step size: 120 nm).

To detect the mitochondrial membrane potential (ΔΨm), neurons were stained for 10 min at 37 °C with 50 nM of the ΔΨm-sensitive, fluorescent dye TMRE85[54]. As a positive control, we pre-incubated neurons for 5 minutes with 5 μM of the OXPHOS uncoupler carbonyl cyanide-4- (trifluoromethoxy) m-chlorophenylhydrazone (CCCP), diluted in complete neurobasal medium. After the incubations, neurons were washed twice with pre-warmed complete neurobasal medium and imaged live using a Zeiss LSM 800 inverted confocal microscope (Carl Zeiss) fitted with a Plan-Apochromat ×63 objective (NA = 1.4). The microscope was equipped with a humidified environmental chamber maintained at 37°C and 5% CO2 to maintain cell viability during live imaging.

Image Acquisition and Morphometric Analysis of the neurons

Cells were visualized using LSM-800 (Zeiss, Oberkochen, Germany) (Lasers: 488, 533, and 633; resolution X = 1024; Y = 1024, and Z = 0.3–0.5 mm; Objectives: 63 : Plan-Apochromat 63 /1.40 Oil DICM27 and 20X : Objective 20X LD Apochromat 20X /0.40, inverted confocal microscope. Microscopy images were acquired at CEMINCO (Centro de Micro y Nanoscopía de Córdoba, Argentina). Post-imaging analysis was done using Fiji-ImageJ (NIH, United States) [91].

For neurite length measurements, images of GFP-transfected neurons were acquired at DIV3 (under control conditions and conditions involving CREB3L1 silencing or overexpression) using a Zeiss LSM 800 confocal microscope. In each case, a maximum intensity projection was generated to highlight the GFP signal, and background was subtracted. The images

shown in Figures 5H and 5L correspond to the GFP signal and the grayscale binary masks used for morphological analysis. At this stage (stage 3/DIV3), the axonal domain is distinguishable because its length is at least 2 to 3 times that of the minor neurites, in accordance with established protocols (Wilson, Rozés-Salvador, and Cáceres, 2020). Average neurite length is defined as the mean length of all minor neurites per neuron (excluding the axon). Total neurite length corresponds to the sum of all neurites (axon + minor neurites). Neurite lengths (axon and minor neurites) were quantified using the segmented line tool in Fiji-ImageJ.

For Tau-1 pattern analysis (Figs. 5R and 5S), images were processed using Fiji-ImageJ. Maximum fluorescence intensity was projected using the Fiji Z-project plugin. Subsequently, images were multiplied by a binary mask generated from the GFP channel to specifically analyze Tau-1 signals within the axons of the transfected neurons.

For *in vivo* migration and morphology measurements (Fig. 6), multiple fields per section were acquired to reconstruct the entire tissue (from the ventricular zone to the cortical plate). The images were then stitched together using the Fiji-ImageJ Stitching plugin. To analyze migration, the embryonic neocortex was divided into four zones (from bottom to top)—ventricular zone (VZ), subventricular zone (SVZ), intermediate zone (IZ), and cortical plate (CP)—and the number of GFP-positive cells in each zone was quantified [63,65] . Within these same zones, the number of cells exhibiting either a multipolar morphology (a soma with multiple surrounding processes) or a bipolar morphology (a soma with two clearly distinguishable processes) was recorded.

Statistics and reproducibility

Quantified data were analyzed using Prism 8 (GraphPad Software). All bar graphs in the figures represent the mean ± SEM from multiple determinations. Each experiment was replicated at least three times on different days. When analyzing groups of data, the results are represented as SuperPlots showing the individual data points in different colors (blue, red, and black), and the mean ± SEM of the means. The Shapiro–Wilk normality test was used to assess whether datasets were normally distributed. Student's t-tests or ANOVA were performed for parametric data. Mann–Whitney or Kruskal–Wallis tests were used for non-parametric data analysis.

Bioinformatics Analyses

RNA-seq data processing and quantification

Raw paired-end RNA-seq reads were processed using the lcdb-wf pipeline (Dale & Fear), a Snakemake-based workflow for standardized high-throughput sequencing analysis. Adapter and low-quality bases were trimmed using cutadapt. Read quality was assessed with FastQC before and after trimming, and FastQ Screen was used to detect cross-species contamination. Trimmed reads were aligned to the human reference genome using the STAR aligner against the GENCODE v47 annotation. Libraries were generated using a strand-specific protocol (dUTP method, fr-firststrand). Ribosomal RNA contamination was assessed by aligning reads against an rRNA reference index using bowtie2. PCR duplicates were flagged with Picard MarkDuplicates, and additional library quality metrics were computed using Picard CollectRnaSeqMetrics and RSeQC. Gene-level read counts were generated using

750 featureCounts (Subread package), and all quality metrics were aggregated and summarized
751 using MultiQC.

752 Differential expression analysis

753 Differential expression analysis was performed using the DESeq2 package (v1.38.0; Love et
754 al., 2014) in R (v4.2.3), as part of the lcdb-wf pipeline. A DESeqDataSet object was
755 constructed from the gene-level count matrix and the sample metadata table, including
756 genotype (WT, L1-KO, L2-KO, DBL-KO) and cell type (iPSC, i3-derived neurons). Log2
757 fold-change estimates were shrunk using the ashr method (v2.2-63; Stephens, 2017). The
758 contrast examined in this study was L1-KO versus WT in i3 neurons. Genes were considered
759 differentially expressed (DEGs) if they had a Benjamini-Hochberg adjusted p-value (padj) <
760 0.05 and an absolute log2 fold-change > 1. Across all samples, 37,599 genes had nonzero
761 expression (baseMean > 0) vs 78932 total. Applying these thresholds identified 700
762 significantly upregulated and 657 significantly downregulated genes in the L1-KO versus
763 WT contrast in i3Neurons. Ensembl gene identifiers were annotated with gene symbols using
764 the org.Hs.eg.db package via AnnotationDbi (v1.60.0).

765 For downstream visualization, the pre-computed results object was loaded into R (v4.5.0).
766 Sample-level relationships were visualized by principal component analysis (PCA) on
767 variance-stabilizing transformed (VST) counts restricted to the top 500 most variable genes
768 (default ntop parameter of DESeq2::plotPCA()). Heatmaps of the most variable genes and of
769 top DEGs ranked by adjusted p-value were generated using the pheatmap package (v1.0.13),
770 with rows scaled to Z-scores of VST counts and Volcano plots were generated using ggplot2
771 (v4.0.3) and ggrepel (v0.9.8), applying the same significance thresholds (padj < 0.05,
772 |log2FC| > 1).

Gene Set Enrichment Analysis (GSEA)

Functional enrichment was assessed by Gene Set Enrichment Analysis (GSEA), using the full ranked list of genes from the DESeq2 output for each contrast, rather than restricting the analysis to a predefined set of significant DEGs. Genes were ranked by the DESeq2 test statistic (Wald statistic), preserving both the direction and magnitude of differential expression. GSEA was performed as part of the lcdb-wf pipeline (R v4.2.3), using a custom wrapper (run_GSEA(), part of the pipeline's internal lcdbwf R package) built on clusterProfiler (v4.6.0), which relies on the fgsea algorithm (v1.24.0) for the calculation of enrichment scores and permutation-based p-values. GSEA was performed against Gene Ontology gene sets — Biological Process (BP) and Cellular Component (CC), using GO.db (v3.16.0) — and against REACTOME pathways, for the contrast L1-KO versus WT in i3 neurons, using gene annotations.

For each gene set category, resulting terms were subsequently split into two subsets according to the sign of the normalized enrichment score (NES): terms enriched among up-regulated genes (positive NES) and terms enriched among down-regulated genes (negative NES). P-values were adjusted for multiple testing using the Benjamini-Hochberg (BH) procedure, and gene sets were considered significantly enriched at an adjusted p-value (FDR) < 0.05. Results were visualized as dot plots (NES on the x-axis, gene set on the y-axis, point size representing gene count, and color representing adjusted p-value on a sequential monochromatic scale) generated with ggplot2 (v4.0.3).

Pathway analysis

All analyses were performed in R (R Core Team). Package versions correspond to the environment in which each analysis step was originally executed, as recorded via sessionInfo().

Funding

This work was funded by the National Council for Scientific Research of Argentina (CONICET, PIP 2021-2023 to CA and CC), SECyT-UNC from the National University of Cordoba (2018–2021 and 2023-2027 to CA), the National Agency for Science (PICT 2019-1625 to CA, PICT 2020-A-00995 to VRS, PICT 2021-00630 to CW), the International Society for Neurochemistry CAEN 1B (VRS and CW individually), and the NIH to JB. VRS, CW, NN, CC and CA are staff scientists of CONICET. EH and APFG are PhD fellows of CONICET.

Acknowledgments

We acknowledge Dr. Pilar Crespo, Cecilia Sampedro, Dr. Gonzalo Quasollo, and Dr. Carlos Mas for technical assistance at the Center for Microscopy and Nanoscopy of Córdoba (CEMINCO, National University of Córdoba). We also thank Dr. Gabriela Furlan and Dr. Noelia Maldonado from the Cellular Culture Facility and Dr. Luciana Reyna from the Molecular Biology Facility of the CIBICI-CONICET-UNC for their assistant and support.

Declaration of Generative AI Use

Gemini (Google) was used exclusively for proofreading and grammatical refinement. The authors retain full responsibility for all scientific content, methodology, and conclusions.

Author contribution

Conceptualization: CA (project genesis and original idea), VR-S. Experiments: VR-S, CW, RDP, VM, EH, LS. Bioinformatics analysis: BF, MS, RKD, TL, NN, APFG. Formal analysis: VR-S, CW, RDP, JB and CA. Funding and resources: VR-S, CW, CC, JB and CA. Supervision: VR-S and CA. Writing the original draft: VR-S and CA. Review and editing: all authors.

References

1. Savaskan, N. E. *et al.* Impaired postnatal development of hippocampal neurons and axon projections in the Emx2–/– mutants. *J. Neurochem.* 83, 1196–1207 (2002).
2. Heins, N. *et al.* Glial cells generate neurons: the role of the transcription factor Pax6. *Nat. Neurosci.* 5, 308–315 (2002).
3. Bertrand, N., Castro, D. S. & Guillemot, F. Proneural genes and the specification of neural cell types. *Nat. Rev. Neurosci.* 3, 517–530 (2002).
4. Bedogni, F. *et al.* Tbr1 regulates regional and laminar identity of postmitotic neurons in developing neocortex. *Proc. Natl. Acad. Sci. U. S. A.* 107, 13129–34 (2010).
5. Burga, A., Casanueva, M. O. & Lehner, B. Predicting mutation outcome from early stochastic variation in genetic interaction partners. *Nature* 480, 250–253 (2011).
6. Kageyama, R., Ohtsuka, T. & Kobayashi, T. The Hes gene family: repressors and oscillators that orchestrate embryogenesis. *Development* 134, 1243–1251 (2007).
7. Zheng, L. *et al.* Parkin functionally interacts with PGC-1α to preserve mitochondria and protect dopaminergic neuron *s*. *Hum. Mol. Genet.* ddw418 (2017) doi:10.1093/hmg/ddw418.
8. Agostini, M. *et al.* Metabolic reprogramming during neuronal differentiation. *Cell Death Differ.* 23, 1502–1514 (2016).
9. Rangaraju, V. *et al.* Pleiotropic Mitochondria: The Influence of Mitochondria on Neuronal Development and Disease. *J. Neurosci.* 39, 8200–8208 (2019).
10. Spinelli, J. B. & Haigis, M. C. The multifaceted contributions of mitochondria to cellular metabolism. *Nat. Cell Biol.* 20, 745–754 (2018).

11. Richter, C. & Kass, G. E. N. Oxidative stress in mitochondria: Its relationship to cellular Ca2+ homeostasis, cell death, proliferation, and differentiation. *Chem. Biol. Interact.* 77, 1–23 (1991).

12. Sheng, Z.-H. & Cai, Q. Mitochondrial transport in neurons: impact on synaptic homeostasis and neurodegeneration. *Nat. Rev. Neurosci.* 13, 77–93 (2012).

13. Vasileiou, P. *et al.* Mitochondrial Homeostasis and Cellular Senescence. *Cells* 8, 686 (2019).

14. Cid-Arregui, A., De Hoop, M. & Dottii, C. G. Mechanisms of neuronal polarity. *Neurobiol. Aging* 16, 239–243 (1995).

15. Dotti, C. G., Sullivan, C. A. & Banker, G. A. *The Establishment of Polarity by Hippocampal Neurons in Culture*. *The Journal of Neuroscience* vol. I (1988).

16. Cáceres, A., Ye, B. & Dotti, C. G. Neuronal polarity: Demarcation, growth and commitment. *Current Opinion in Cell Biology* vol. 24 547–553 Preprint at https://doi.org/10.1016/j.ceb.2012.05.011 (2012).

17. Dent, E. W., Gupton, S. L. & Gertler, F. B. The growth cone cytoskeleton in axon outgrowth and guidance. *Cold Spring Harb. Perspect. Biol.* 3, (2011).

18. Burack, M. A., Silverman, M. A. & Banker, G. The Role of Selective Transport in Neuronal Protein Sorting. *Neuron* 26, 465–472 (2000).

19. Yap, C. C. & Winckler, B. Harnessing the Power of the Endosome to Regulate Neural Development. *Neuron* 74, 440–451 (2012).

20. Takano, T., Xu, C., Funahashi, Y., Namba, T. & Kaibuchi, K. Neuronal polarization. *Development* 142, 2088–2093 (2015).

21. Iwata, R., Casimir, P. & Vanderhaeghen, P. Mitochondrial dynamics in postmitotic cells regulate neurogenesis. *Science* 369, 858–862 (2020).

22. Chen, W., Zhao, H. & Li, Y. Mitochondrial dynamics in health and disease: mechanisms and potential targets. *Signal Transduct. Target. Ther.* 8, 333 (2023).

23. Seager, R., Lee, L., Henley, J. M. & Wilkinson, K. A. Mechanisms and roles of mitochondrial localisation and dynamics in neuronal function. *Neuronal Signal.* 4, NS20200008 (2020).

24. Fox, R. M. & Andrew, D. J. Transcriptional regulation of secretory capacity by bZip transcription factors. *Frontiers in Biology* vol. 10 28–51 Preprint at https://doi.org/10.1007/s11515-014-1338-7 (2015).

25. Sampieri, L., Di Giusto, P. & Alvarez, C. CREB3 Transcription Factors: ER-Golgi Stress Transducers as Hubs for Cellular Homeostasis. *Front. Cell Dev. Biol.* 7, (2019).

26. Saito, A., Omura, I. & Imaizumi, K. CREB3L1/OASIS: cell cycle regulator and tumor suppressor. *FEBS J.* 291, 4853–4866 (2024).

27. He, D. *et al.* Chd7 cooperates with Sox10 and regulates the onset of CNS myelination and remyelination. *Nat. Neurosci.* 19, 678–689 (2016).

28. Sampieri, L., Funes Chabán, M., Di Giusto, P., Rozés-Salvador, V. & Alvarez, C. CREB3L2 Modulates Nerve Growth Factor-Induced Cell Differentiation. *Front. Mol. Neurosci.* 14, (2021).

29. Honma, Y. *et al.* Identification of a novel gene, OASIS, which encodes for a putative CREB/ATF family transcription factor in the long-term cultured astrocytes and gliotic tissue. *Molecular Brain Research* 69, 93–103 (1999).

30. Greenwood, M. *et al.* Transcription factor CREB3L1 mediates cAMP and glucocorticoid regulation of arginine vasopressin gene transcription in the rat hypothalamus. *Mol. Brain* 8, 68 (2015).

31. Greenwood, M. *et al.* Transcription factor CREB3L1 regulates vasopressin gene expression in the rat hypothalamus. *J. Neurosci.* 34, 3810–20 (2014).

32. Greenwood, M. *et al.* Transcription factor Creb3l1 maintains proteostasis in neuroendocrine cells. *Mol. Metab.* 63, 101542 (2022).

33. García, I. A. *et al.* CREB3L1-mediated functional and structural adaptation of the secretory pathway in hormone-stimulated thyroid cells. *J. Cell Sci.* https://doi.org/10.1242/jcs.211102 (2017) doi:10.1242/jcs.211102.

34. Di Giusto, P. *et al.* Transcription Factor CREB3L1 Regulates the Expression of the Sodium/Iodide Symporter (NIS) in Rat Thyroid Follicular Cells. *Cells* 11, 1314 (2022).

35. Wang, C. *et al.* Scalable Production of iPSC-Derived Human Neurons to Identify Tau-Lowering Compounds by High-Content Screening. *Stem Cell Reports* 9, 1221–1233 (2017).

36. De Pace, R. *et al.* Messenger RNA transport on lysosomal vesicles maintains axonal mitochondrial homeostasis and prevents axonal degeneration. *Nat. Neurosci.* 27, 1087–1102 (2024).

37. Cavaco, J. & Carvalhal, S. Non-canonical roles of mitotic proteins in cortical neurons. *Trends Neurosci.* 48, 495–507 (2025).

38. Ferhat, L. *et al.* Expression of the Mitotic Motor Protein Eg5 in Postmitotic Neurons: Implications for Neuronal Development. *The Journal of Neuroscience* 18, 7822–7835 (1998).

39. Zhao, G. *et al.* Kinetochore proteins control microtubule dynamics in postmitotic neurons to regulate the formation of dendritic spines. *Proceedings of the National Academy of Sciences* 123, (2026).

40. Nwagbara, B. U. *et al.* TACC3 is a microtubule plus end–tracking protein that promotes axon elongation and also regulates microtubule plus end dynamics in multiple embryonic cell types. *Mol. Biol. Cell* 25, 3350–3362 (2014).

41. Muralidharan, H. *et al.* KIFC1 Regulates the Trajectory of Neuronal Migration. *The Journal of Neuroscience* 42, 2149–2165 (2022).

42. Fernandopulle, M. S. *et al.* Transcription Factor–Mediated Differentiation of Human iPSCs into Neurons. *Curr. Protoc. Cell Biol.* 79, (2018).

43. Kaech, S. & Banker, G. Culturing hippocampal neurons. *Nat. Protoc.* 1, 2406–2415 (2006).

44. Banker, G. & Goslin, K. Developments in neuronal cell culture. *Nature* 336, 185–6 (1988).

45. Wu, Z. *et al.* Mechanisms controlling mitochondrial biogenesis and respiration through the thermogenic coactivator PGC-1. *Cell* 98, 115–24 (1999).

46. Misko, A., Jiang, S., Wegorzewska, I., Milbrandt, J. & Baloh, R. H. Mitofusin 2 is necessary for transport of axonal mitochondria and interacts with the Miro/Milton complex. *J. Neurosci.* 30, 4232–40 (2010).

47. Su, J. *et al.* Structure of the intact Tom20 receptor in the human translocase of the outer membrane complex. *PNAS nexus* 3, pgae269 (2024).

48. Neikirk, K. *et al.* MitoTracker: A useful tool in need of better alternatives. *Eur. J. Cell Biol.* 102, 151371 (2023).

49. Griparic, L., van der Wel, N. N., Orozco, I. J., Peters, P. J. & van der Bliek, A. M. Loss of the Intermembrane Space Protein Mgm1/OPA1 Induces Swelling and Localized Constrictions along the Lengths of Mitochondria. *Journal of Biological Chemistry* 279, 18792–18798 (2004).

50. Palmer, C. S. *et al.* MiD49 and MiD51, new components of the mitochondrial fission machinery. *The EMBO Reports* 12, 565–573 (2011).

51. Cieri, D. *et al.* Tau localises within mitochondrial sub-compartments and its caspase cleavage affects ER-mitochondria interactions and cellular Ca2+ handling.

Biochimica et Biophysica Acta (BBA) - Molecular Basis of Disease 1864, 3247–3256 (2018).

52. Bando, Y., Hirano, T. & Tagawa, Y. Dysfunction of KCNK potassium channels impairs neuronal migration in the developing mouse cerebral cortex. *Cereb. Cortex* 24, 1017–29 (2014).

53. Almutawa, W. *et al.* The R941L mutation in MYH14 disrupts mitochondrial fission and associates with peripheral neuropathy. *EBioMedicine* 45, 379–392 (2019).

54. Crowley, L. C., Christensen, M. E. & Waterhouse, N. J. Measuring Mitochondrial Transmembrane Potential by TMRE Staining. *Cold Spring Harb. Protoc.* 2016, (2016).

55. Benowitz, L. I. & Routtenberg, A. GAP-43: an intrinsic determinant of neuronal development and plasticity. *Trends Neurosci.* 20, 84–91 (1997).

56. Kunda, P., Paglini, G., Quiroga, S., Kosik, K. & Cáceres, A. Evidence for the Involvement of Tiam1 in Axon Formation. *The Journal of Neuroscience* 21, 2361–2372 (2001).

57. Ferreira, A. & Caceres, A. Expression of the Class III β-tubulin isotype in developing neurons in culture. *J. Neurosci. Res.* 32, 516–529 (1992).

58. Francis, F. *et al.* Doublecortin is a developmentally regulated, microtubule-associated protein expressed in migrating and differentiating neurons. *Neuron* 23, 247–56 (1999).

59. Izant, J. G. & McIntosh, J. R. Microtubule-associated proteins: a monoclonal antibody to MAP2 binds to differentiated neurons. *Proceedings of the National Academy of Sciences* 77, 4741–4745 (1980).

60. Bentley, M. & Banker, G. The cellular mechanisms that maintain neuronal polarity. *Nature Publishing Group* https://doi.org/10.1038/nrnnrn.2016.100 (2016) doi:10.1038/nrnnrn.2016.100.

61. Kempf, M., Clement, A., Faissner, A., Lee, G. & Brandt, R. Tau Binds to the Distal Axon Early in Development of Polarity in a Microtubule- and Microfilament-Dependent Manner. *The Journal of Neuroscience* 16, 5583–5592 (1996).

62. Arimura, N. & Kaibuchi, K. Key regulators in neuronal polarity. *Neuron* vol. 48 881–884 Preprint at https://doi.org/10.1016/j.neuron.2005.11.007 (2005).

63. Wilson, C., Rozés-Salvador, V. & Cáceres, A. Protocol for Evaluating Neuronal Polarity in Murine Models. *STAR Protoc.* 1, (2020).

64. Noctor, S. C., Martinez-Cerdeño, V., Ivic, L. & Kriegstein, A. R. Cortical neurons arise in symmetric and asymmetric division zones and migrate through specific phases. *Nat. Neurosci.* 7, 136–144 (2004).

65. Rozés-Salvador, V., Wilson, C., Olmos, C., Gonzalez-Billault, C. & Conde, C. Fine-Tuning the TGFβ Signaling Pathway by SARA During Neuronal Development. *Front. Cell Dev. Biol.* 8, (2020).

66. Saito, A. *et al.* p53-independent tumor suppression by cell-cycle arrest via CREB/ATF transcription factor OASIS. *Cell Rep.* 42, 112479 (2023).

67. Kahn, O. I., Sharma, V., González-Billault, C. & Baas, P. W. Effects of kinesin-5 inhibition on dendritic architecture and microtubule organization. *Mol. Biol. Cell* 26, 66–77 (2015).

68. Ying, Z., Misra, V. & Verge, V. M. K. Sensing nerve injury at the axonal ER: Activated Luman/CREB3 serves as a novel axonally synthesized retrograde regeneration signal. *Proc. Natl. Acad. Sci. U. S. A.* 111, 16142–16147 (2014).

69. Saito, T. In vivo electroporation in the embryonic mouse central nervous system. *Nat. Protoc.* 1, 1552–1558 (2006).

70. Hirotsune, S. *et al.* Graded reduction of Pafah1b1 (Lis1) activity results in neuronal migration defects and early embryonic lethality. *Nat. Genet.* 19, 333–9 (1998).

71. Gleeson, J. G., Lin, P. T., Flanagan, L. A. & Walsh, C. A. Doublecortin is a microtubule-associated protein and is expressed widely by migrating neurons. *Neuron* 23, 257–71 (1999).

72. Cooper, J. A. Mechanisms of cell migration in the nervous system. *Journal of Cell Biology* 202, 725–734 (2013).

73. Cooper, J. A. Molecules and mechanisms that regulate multipolar migration in the intermediate zone. *Front. Cell. Neurosci.* 8, (2014).

74. Tabata, H. & Nakajima, K. Multipolar Migration: The Third Mode of Radial Neuronal Migration in the Developing Cerebral Cortex. *The Journal of Neuroscience* 23, 9996–10001 (2003).

75. Whalley, H. J. *et al.* Cdk1 phosphorylates the Rac activator Tiam1 to activate centrosomal Pak and promote mitotic spindle formation. *Nat. Commun.* 6, 7437 (2015).

76. Harada, A. *et al.* Altered microtubule organization in small-calibre axons of mice lacking tau protein. *Nature* 369, 488–491 (1994).

77. Namba, T. *et al.* Pioneering Axons Regulate Neuronal Polarization in the Developing Cerebral Cortex. *Neuron* 81, 814–829 (2014).

78. Witte, H. & Bradke, F. The role of the cytoskeleton during neuronal polarization. *Curr. Opin. Neurobiol.* 18, 479–487 (2008).

79. Kondo, S. *et al.* OASIS, a CREB/ATF-family member, modulates UPR signalling in astrocytes. *Nat. Cell Biol.* 7, 186–194 (2005).

80. Murakami, T. *et al.* Signalling mediated by the endoplasmic reticulum stress transducer OASIS is involved in bone formation. *Nat. Cell Biol.* 11, 1205–1211 (2009).

81. Fox, R. M. & Andrew, D. J. Transcriptional regulation of secretory capacity by bZip transcription factors. *Front. Biol. (Beijing).* 10, 28–51 (2015).

82. Ristow, M. & Schmeisser, K. Mitohormesis: Promoting Health and Lifespan by Increased Levels of Reactive Oxygen Species (ROS). *Dose-Response* 12, (2014).

83. Khacho, M. *et al.* Mitochondrial Dynamics Impacts Stem Cell Identity and Fate Decisions by Regulating a Nuclear Transcriptional Program. *Cell Stem Cell* 19, 232–247 (2016).

84. Paillusson, S. *et al.* There's Something Wrong with my MAM; the ER–Mitochondria Axis and Neurodegenerative Diseases. *Trends Neurosci.* 39, 146–157 (2016).

85. Vance, J. E. MAM (mitochondria-associated membranes) in mammalian cells: Lipids and beyond. *Biochimica et Biophysica Acta (BBA) - Molecular and Cell Biology of Lipids* 1841, 595–609 (2014).

86. Hinton, A. *et al.* ATF4-dependent increase in mitochondrial-endoplasmic reticulum tethering following OPA1 deletion in skeletal muscle. *J. Cell. Physiol.* 239, (2024).

87. Cartes-Saavedra, B. *et al.* OPA1 Modulates Mitochondrial Ca2+ Uptake Through ER-Mitochondria Coupling. *Front. Cell Dev. Biol.* 9, (2022).

88. Keller, R. B. *et al.* Monoallelic and biallelic CREB3L1 variant causes mild and severe osteogenesis imperfecta, respectively. *Genetics in Medicine* 20, 411–419 (2018).

89. Zheng, X. *et al.* Metabolic reprogramming during neuronal differentiation from aerobic glycolysis to neuronal oxidative phosphorylation. *Elife* 5, (2016).

90. Denard, B. *et al.* The Membrane-Bound Transcription Factor CREB3L1 Is Activated in Response to Virus Infection to Inhibit Proliferation of Virus-Infected Cells. *Cell Host Microbe* 10, 65–74 (2011).

91. Schindelin, J. *et al.* Fiji: an open-source platform for biological-image analysis. *Nat. Methods* 9, 676–682 (2012).

Figure 1:

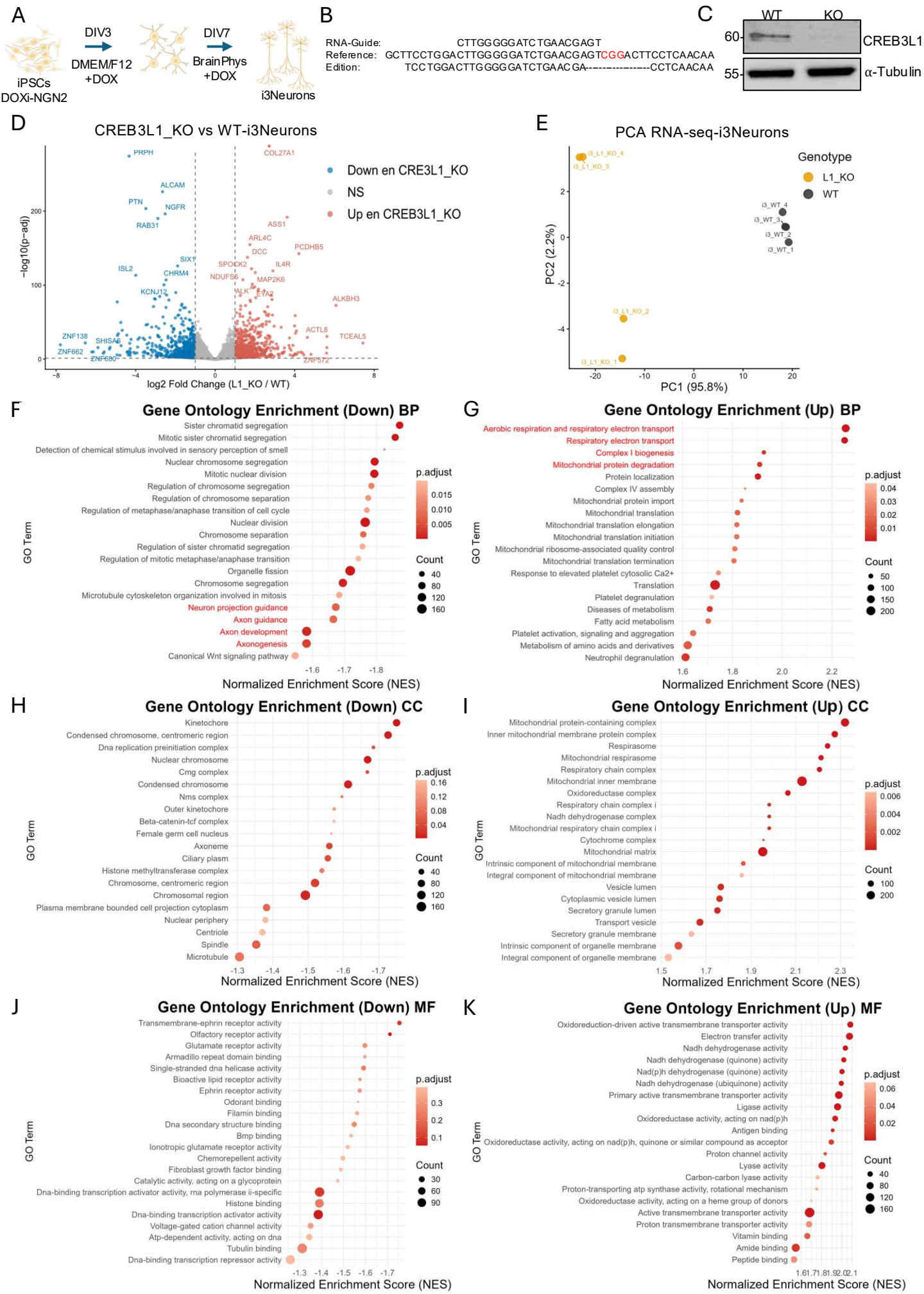
A
iPSCs
DOXi-NGN2
DIV3
DMEM/F12
+DOX
DIV7
BrainPhys
+DOX
i3Neurons
B
RNA-Guide: CTTGGGGGATCTGAACGAGT
Reference: GCTTCCTGGACTTGGGGGATCTGAACGAGTCGGGACTTCCTCAACAA
Edition: TCCTGGACTTGGGGGATCTGAACGA----------CCTCAACAA
C
WT
KO
60
55
CREB3L1
α-Tubulin
D
CREB3L1_KO vs WT-i3Neurons
Down en CRE3L1_KO
NS
Up en CREB3L1_KO
−log10(p−adj)
log2 Fold Change (L1_KO / WT)
PRPH
COL27A1
ALCAM
PTN
NGFR
RAB31
ASS1
ARL4C
DCC
PCDHB5
SIX1
ISL2
CHRM4
SPOCK2
IL4R
NDUFS6
MAP2K6
KCNJ12
ALK
EYA2
ALKBH3
ACTL8
TCEAL5
ZNF138
SHISA6
ZNF662
ZNF680
ZNF572
E
PCA RNA-seq-i3Neurons
Genotype
L1_KO
WT
i3_L1_KO_4
i3_L1_KO_3
i3_WT_4
i3_WT_3
i3_WT_2
i3_WT_1
i3_L1_KO_2
i3_L1_KO_1
PC2 (2.2%)
PC1 (95.8%)
F
Gene Ontology Enrichment (Down) BP
Sister chromatid segregation
Mitotic sister chromatid segregation
Detection of chemical stimulus involved in sensory perception of smell
Nuclear chromosome segregation
Mitotic nuclear division
Regulation of chromosome segregation
Regulation of chromosome separation
Regulation of metaphase/anaphase transition of cell cycle
Nuclear division
Chromosome separation
Regulation of sister chromatid segregation
Regulation of mitotic metaphase/anaphase transition
Organelle fission
Chromosome segregation
Microtubule cytoskeleton organization involved in mitosis
Neuron projection guidance
Axon guidance
Axon development
Axonogenesis
Canonical Wnt signaling pathway
GO Term
p.adjust
Count
Normalized Enrichment Score (NES)
G
Gene Ontology Enrichment (Up) BP
Aerobic respiration and respiratory electron transport
Respiratory electron transport
Complex I biogenesis
Mitochondrial protein degradation
Protein localization
Complex IV assembly
Mitochondrial protein import
Mitochondrial translation
Mitochondrial translation elongation
Mitochondrial translation initiation
Mitochondrial ribosome-associated quality control
Mitochondrial translation termination
Response to elevated platelet cytosolic Ca2+
Translation
Platelet degranulation
Diseases of metabolism
Fatty acid metabolism
Platelet activation, signaling and aggregation
Metabolism of amino acids and derivatives
Neutrophil degranulation
H
Gene Ontology Enrichment (Down) CC
Kinetochore
Condensed chromosome, centromeric region
Dna replication preinitiation complex
Nuclear chromosome
Cmg complex
Condensed chromosome
Nms complex
Outer kinetochore
Beta-catenin-tcf complex
Female germ cell nucleus
Axoneme
Ciliary plasm
Histone methyltransferase complex
Chromosome, centromeric region
Chromosomal region
Plasma membrane bounded cell projection cytoplasm
Nuclear periphery
Centriole
Spindle
Microtubule
I
Gene Ontology Enrichment (Up) CC
Mitochondrial protein-containing complex
Inner mitochondrial membrane protein complex
Respirasome
Mitochondrial respirasome
Respiratory chain complex
Mitochondrial inner membrane
Oxidoreductase complex
Respiratory chain complex i
Nadh dehydrogenase complex
Mitochondrial respiratory chain complex i
Cytochrome complex
Mitochondrial matrix
Intrinsic component of mitochondrial membrane
Integral component of mitochondrial membrane
Vesicle lumen
Cytoplasmic vesicle lumen
Secretory granule lumen
Transport vesicle
Secretory granule membrane
Intrinsic component of organelle membrane
Integral component of organelle membrane
J
Gene Ontology Enrichment (Down) MF
Transmembrane-ephrin receptor activity
Olfactory receptor activity
Glutamate receptor activity
Armadillo repeat domain binding
Single-stranded dna helicase activity
Bioactive lipid receptor activity
Ephrin receptor activity
Odorant binding
Filamin binding
Dna secondary structure binding
Bmp binding
Ionotropic glutamate receptor activity
Chemorepellent activity
Fibroblast growth factor binding
Catalytic activity, acting on a glycoprotein
Dna-binding transcription activator activity, rna polymerase ii-specific
Histone binding
Dna-binding transcription activator activity
Voltage-gated cation channel activity
Atp-dependent activity, acting on dna
Tubulin binding
Dna-binding transcription repressor activity
K
Gene Ontology Enrichment (Up) MF
Oxidoreduction-driven active transmembrane transporter activity
Electron transfer activity
Nadh dehydrogenase activity
Nadh dehydrogenase (quinone) activity
Nad(p)h dehydrogenase (quinone) activity
Nadh dehydrogenase (ubiquinone) activity
Primary active transmembrane transporter activity
Ligase activity
Oxidoreductase activity, acting on nad(p)h
Antigen binding
Oxidoreductase activity, acting on nad(p)h, quinone or similar compound as acceptor
Proton channel activity
Lyase activity
Carbon-carbon lyase activity
Proton-transporting atp synthase activity, rotational mechanism
Oxidoreductase activity, acting on a heme group of donors
Active transmembrane transporter activity
Proton transmembrane transporter activity
Vitamin binding
Amide binding
Peptide binding

Figure Legends

Figure 1: CREB3L1 depletion in i3 Neurons and RNA-seq analysis. A: iPSCs were differentiated for DIV3 in DMEM/F12 medium supplemented with doxycycline (DOX) and further cultured for DIV7 in BrainPhys medium containing DOX. **B:** Schematic representation of the sgRNA sequence and editing site. **C:** SDS-PAGE and immunoblot of WT and CREB3L1_KO iPSCs probed for CREB3L1 and Tubulin (loading control). **D:** Volcano of up- and downregulated genes in CREB3L1_KO vs WT i3Neurons. **E:** Principal Component Analysis (PCA) of the CREB3L1_KO and WT i3Neuron samples used for RNA-seq analysis, showing the variance explained by PC1 and PC2. **F-I:** Gene set enrichment analysis (GSEA) of Gene Ontology (GO) terms in CREB3L1_KO i3Neurons compared to WT controls. Biological Process (BP) terms enriched among downregulated (F) and upregulated (G), Cellular Component (CC) terms associated with downregulated (H) and upregulated (I) genes and Molecular Function (MF) terms associated with downregulated (J) and upregulated (K) genes. The GO BP terms highlighted in red in F and G represent the axon-related and mitochondrial processes, respectively, selected for subsequent gene-level analysis in Fig. 2C and D.

Figure 2

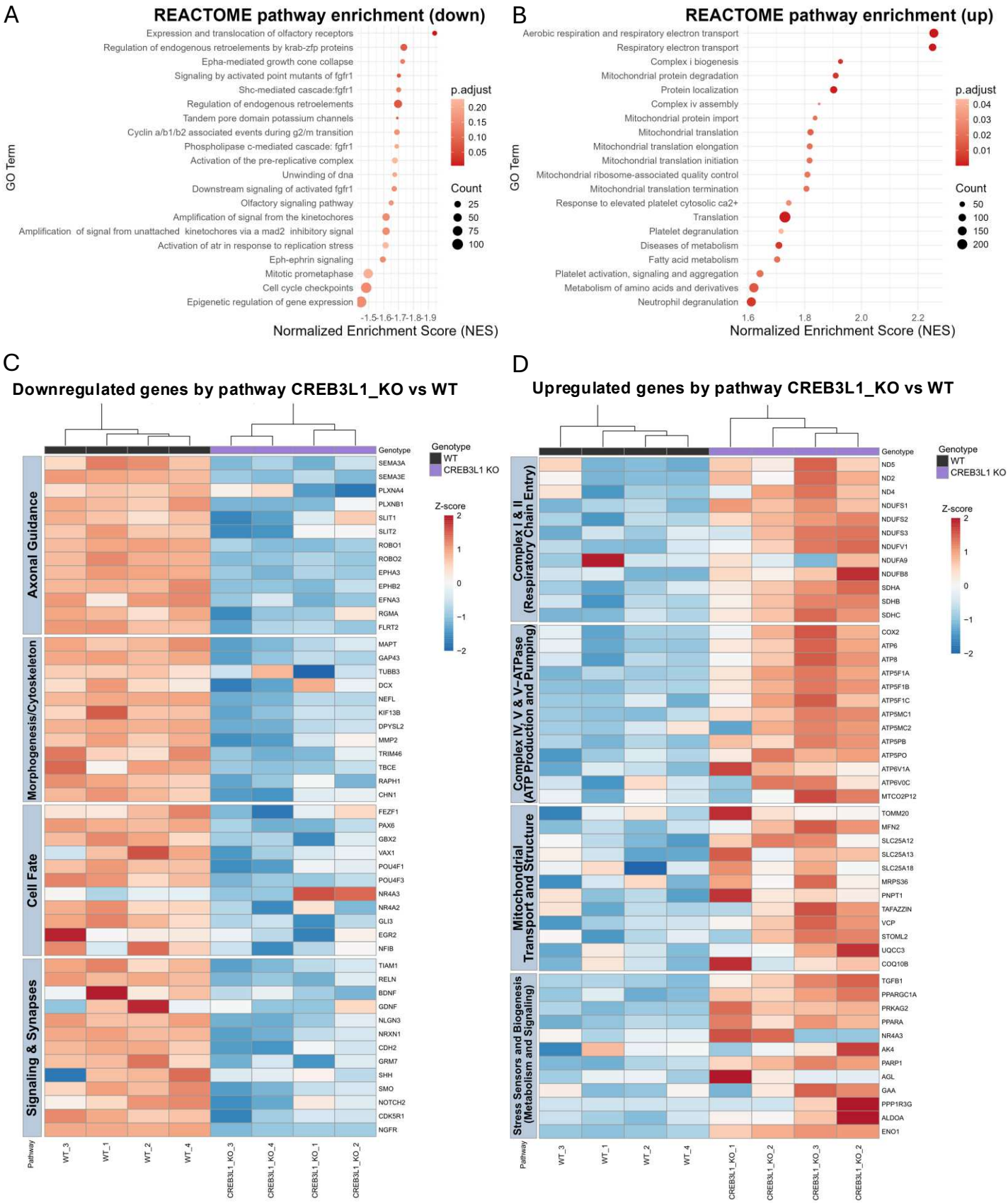

Figure 2: CREB3L1 deficiency compromises cytoskeleton integrity and the expression of neuronal maturation markers. A and B: GSEA of REACTOME terms showing the metabolic pathways of the downregulated (A) and upregulated (B) genes regulated in CREB3L1_KO i3 Neurons compared to WT controls. **C:** Heatmap of 50 of the downregulated genes associated with the GO BP terms neuron projection, axon development, axon guidance, and axonogenesis in CREB3L1_KO i3Neurons. **D:** Heat map of 50 upregulated genes associated with the GO BP terms aerobic respiration and respiratory electron transport, respiratory electron transport, complex I biogenesis, and mitochondrial protein degradation in i3 CREB3L1_KO neurons.

Figure 3

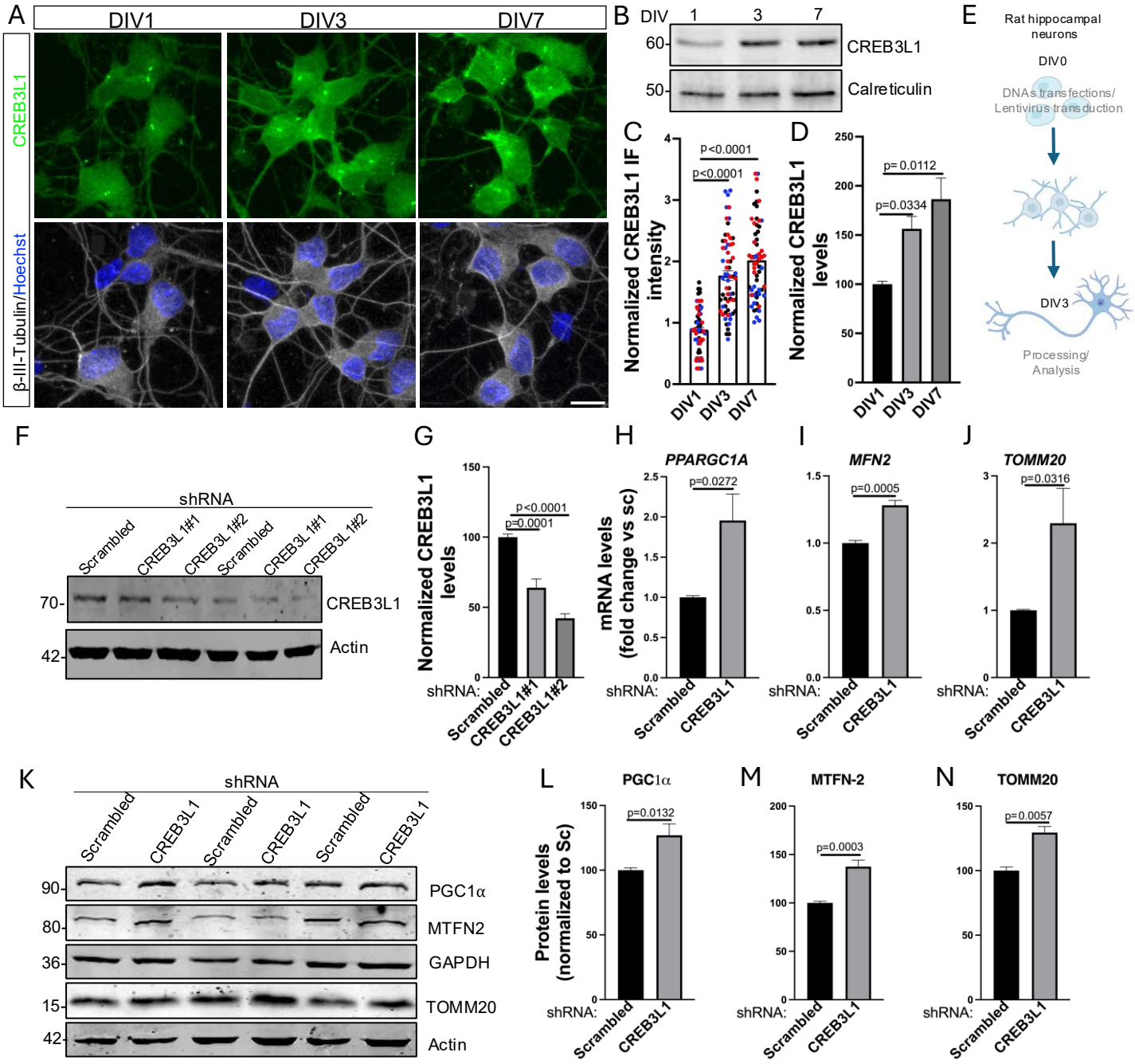

Figure 3: Loss of CREB3L1 function increased mitochondrial mass and biogénesis. A: Representative images of hippocampal neurons 1, 3, and 7DIV immunolabeled against CREB3L1, and ß-III-tubulin, and Hoechst to label the nuclei. **B:** SDS-PAGE and immunoblot of protein extracts of neurons from 1, 3 and 7DIV and probed for CREB3L1. Calreticulin was used as loading controls **C:** Quantification of fluorescence intensity from confocal images using ImageJ. Data represent the mean ± SEM from three independent experiments (n=3). Anova; Kruskal-Wallis. Scale: 20 µm. **D:** Quantification of normalized CREB3L1 protein levels. One-way ANOVA with Dunnett's multiple comparisons test. Data represent the mean ± SEM from three independent experiments (n=3). **E:** Schematic representation of the workflow: hippocampal neurons were transfected or transduced with lentivirus immediately after seeding, and sample processing or immunofluorescence analysis was performed at 3 DIV. **F:** SDS-PAGE and immunoblot of neurons from 3DIV infected with lentiviral particles carrying shScramble or two different sequences of shCREB3L1 (#1 and #2) and probed for CREB3L1 and actin (loading control). **G:** Quantification of normalized CREB3L1 protein levels. One-way ANOVA with Dunnett's multiple comparisons test. Data represent the mean ± SEM from three independent experiments (n=3). **H-J:** Transcriptional analysis of *PPARGC1A* (PGC1α) (F), *MFN2* (G), and *TOMM20* (H) was performed by reverse transcription and quantitative PCR (qRT-PCR). mRNAs from hippocampal neurons infected with lentiviral particles carrying shScramble or shCREB3L1 was isolated. Fold changes were estimated using the ΔΔCT method. Expression levels were normalized against GAPDH and expressed relative to the shScramble condition. Student's t-test. **K:** SDS-PAGE and immunoblot of protein extracts of neurons infected with lentiviral particles containing shScramble or shCREB3L1 and probed for PGC1α, MTFN2, and TOMM20. GAPDH and actin were used as loading controls. **L-N:** Quantification of the normalized intensity of PGC1α (J), MTFN2 (K), and TOMM20 (L). Student's t-test. Data represent the mean ± SEM from three independent experiments (n=3).

Figure 4

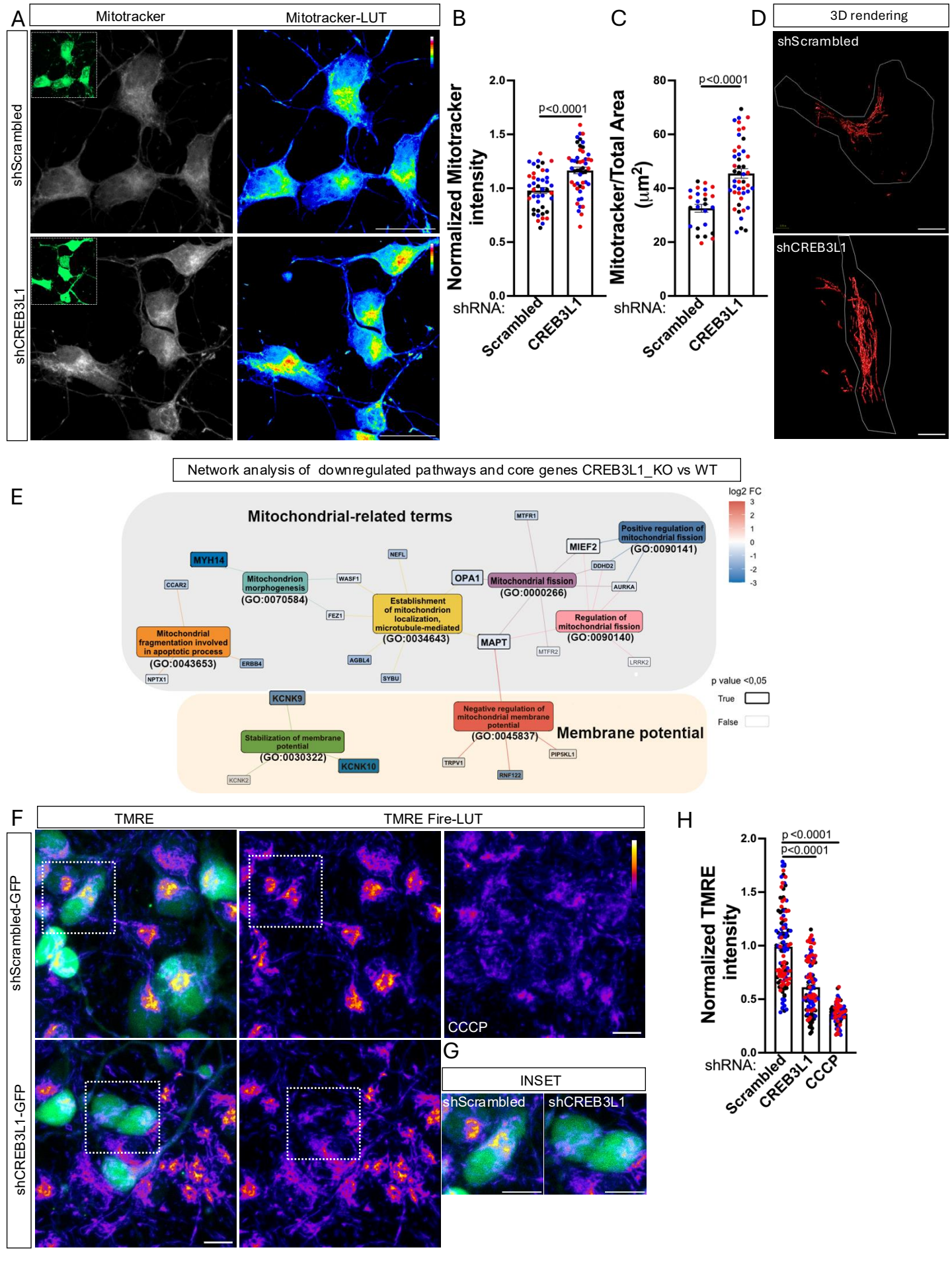
A
Mitotracker
Mitotracker-LUT
shScrambled
shCREB3L1
B
Normalized Mitotracker intensity
p<0.0001
shRNA:
Scrambled
CREB3L1
C
Mitotracker/Total Area (µm²)
p<0.0001
shRNA:
Scrambled
CREB3L1
D
3D rendering
shScrambled
shCREB3L1
Network analysis of downregulated pathways and core genes CREB3L1_KO vs WT
E
Mitochondrial-related terms
log2 FC
MYH14
Mitochondrion morphogenesis (GO:0070584)
Mitochondrial fragmentation involved in apoptotic process (GO:0043653)
Establishment of mitochondrion localization, microtubule-mediated (GO:0034643)
OPA1
Mitochondrial fission (GO:0000266)
MIEF2
Positive regulation of mitochondrial fission (GO:0090141)
Regulation of mitochondrial fission (GO:0090140)
MAPT
p value <0,05
True
False
KCNK9
Stabilization of membrane potential (GO:0030322)
KCNK10
Negative regulation of mitochondrial membrane potential (GO:0045837)
Membrane potential
F
TMRE
TMRE Fire-LUT
shScrambled-GFP
shCREB3L1-GFP
CCCP
G
INSET
shScrambled
shCREB3L1
H
Normalized TMRE intensity
p<0.0001
p<0.0001
shRNA:
Scrambled
CREB3L1
CCCP

Figure 4: Loss of CREB3L1 function impairs mitochondrial membrane potential. **A:** Representative images of DIV3 hippocampal neurons infected with shScrambled or shCREB3L1, incubated with Mitotracker, and fixed. The lower-left insets show the efficiency of lentivirus infection. For better visualization, the Mitotracker marker is also shown in Fire-LUT, where warmer colors indicate higher intensity and cooler colors indicate lower intensity. **B-C:** Quantification of the normalized mitotracker intensity of shCREB3L1 neurons compared to shScrambled (B) and of the area occupied by the mitotracker normalized with the total cell area (C). Student's t-test, Mann-Whitney test. Data represent the mean ± SEM from three independent experiments (n=3). **D:** Representative 3D rendering images obtained in Airy-Scan of neurons infected with shScrambled and shCREB3L1 showing the distribution of the mitochondrial network. **E:** Representative network image illustrating GO BP and key DEGs involved in mitochondrial pathways. Colored nodes represent significantly enriched GO terms. Node color intensity corresponds to the expression change ($\log_2$ FC) in CREB3L1_KO i3Neurons compared to WT cells. Edges represent functional associations or shared connections between pathways and genes. **F:** Representative images of DIV3 hippocampal neurons infected with shScrambled or shCREB3L1, and treatment with TMRE. The panel shows the merge between infected cells expressing GFP and the TMRE label in Fire-LUT for better visualization. The TMRE channel alone is also shown. Neurons were pre-treated with CCCP as a positive control. Scale bar: 10 µm. **G:** Inset of the white boxes showing the merge of TMRE-infected cells. Scale bar: 10 µm. **H:** Quantification of the normalized TMRE intensity of shCREB3L1 neurons and pre-treated with CCCP compared to shScrambled. Anova and Kruskal-Wallis test. Data represent the mean ± SEM from three independent experiments (n=3).

Figure 5

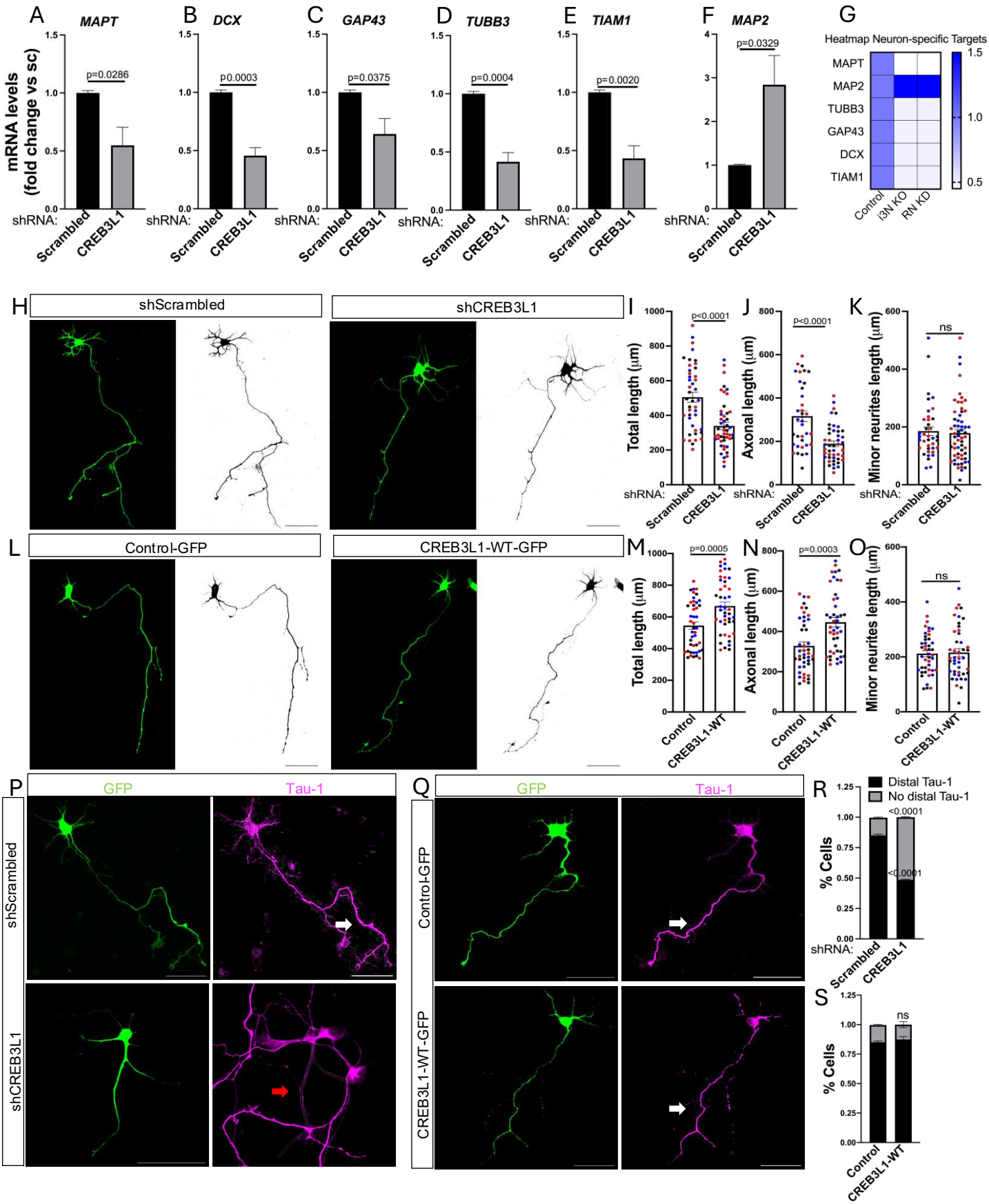
A
MAPT
B
DCX
C
GAP43
D
TUBB3
E
TIAM1
F
MAP2
mRNA levels (fold change vs sc)
p=0.0286
p0.0003
p=0.0375
p=0.0004
p=0.0020
p=0.0329
shRNA:
Scrambled
CREB3L1
G
Heatmap Neuron-specific Targets
MAPT
MAP2
TUBB3
GAP43
DCX
TIAM1
Control
i3N KO
RN KD
H
shScrambled
shCREB3L1
I
Total length (µm)
p<0.0001
J
Axonal length (µm)
p<0.0001
K
Minor neurites length (µm)
ns
L
Control-GFP
CREB3L1-WT-GFP
M
Total length (µm)
p=0.0005
N
Axonal length (µm)
p=0.0003
O
Minor neurites length (µm)
ns
Control
CREB3L1-WT
P
GFP
Tau-1
shScrambled
shCREB3L1
Q
GFP
Tau-1
Control-GFP
CREB3L1-WT-GFP
R
Distal Tau-1
No distal Tau-1
% Cells
<0.0001
<0.0001
S
% Cells
ns

Figure 5: CREB3L1 regulates neurite growth and axon specification in hippocampal neurons. A-F: Transcriptional analysis of *MAPT* (Tau) (A), *Doublecortin* (DCX) (B), *GAP43* (C), *TUBB3* (β3-tubulin) (D), *TIAM1* (E), and *MAP2* (F) was performed by reverse transcription and quantitative PCR (qRT-PCR). mRNAs from hippocampal neurons infected with lentiviral particles carrying shScrambled or shCREB3L1. Fold changes were estimated using the ΔΔCT method. Expression levels were normalized against GAPDH and expressed relative to the shScrambled condition. Student's t-test. Data represent the mean ± SEM from three independent experiments (n=3). **J:** Heatmap summarizing Neuron-specific targets mRNA fold changes between control, i3Neurons CREB3L1-KO (i3N KO), and rat neurons shCREB3L1(KD) (RN KD). Colors reflect the gene expression patterns across each cell model. **H:** Representative images of DIV3 GFP-positive hippocampal neurons expressing shScrambled or shCREB3L1, also visualizing their binary masks. **I-K:** Quantification of total length (I), axonal length (J), and minor neurite length (M) using ImageJ. **L:** Representative images of GFP-positive hippocampal neurons expressing control or CREB3L1-WT, also visualizing their binary masks. **M-O:** Quantification of total length (F), axonal length (N), and minor neurite length (O) of shCREB3L1 neurons compared to shScrambled. Student's t-test, Mann-Whitney test. Data represent the mean ± SEM from three independent experiments (n=3). **P-Q:** Representative images of DIV3 GFP-positive hippocampal neurons showing a z-stack maximal projection of microtubule-associated protein Tau-1 (magenta). The image is the result of multiplying each channel by a binary mask determined using the GFP channel. The panels show neurons expressing shScrambled or shCREB3L1 (P) and neurons expressing Control and CREB3L1-WT (Q). White arrows show the presence of distal Tau-1; red arrow show the lack of distal Tau-1 in the axon. Scale bar: 50μm. **R-S:** Quantification of the percentage of cells exhibiting the characteristic Tau-1 pattern in the axon versus those not exhibiting it. Two-way ANOVA. Data represent the mean ± SEM from three independent experiments (n=3). Scale bar: 50μm.

Figure 6

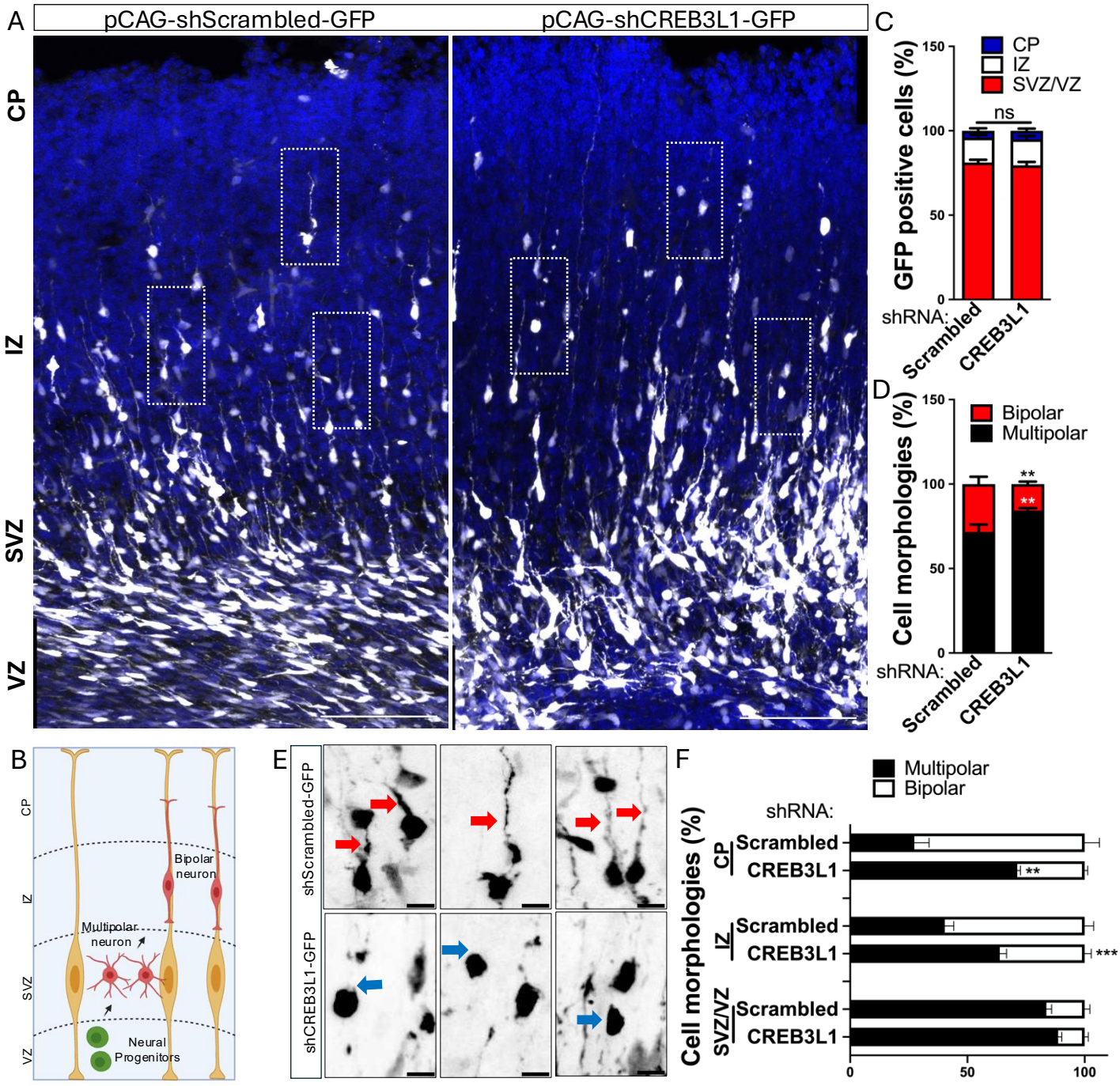

Figure 6: CREB3L1 regulates the multipolar-to-bipolar transition in the developing cerebral cortex. A: Representative E18 coronal slices of brain cortices after in utero electroporation (IUE) of embryonic brains at E15, expressing pCAG-shScrambled-GFP or pCAG-shCREB3L1-GFP and immunostained for DAPI (blue). Scale bar: 100 µm. Three days after IUE (E18), brains were fixed and sectioned for confocal imaging. Cortical layers are defined as ventricular/subventricular zone (VZ/SVZ), intermediate zone (IZ), and cortical plate (CP). **B:** Representative diagram of the layers of the cerebral cortex and the multipolar-bipolar transition that neurons undergo in order to migrate. **C:** Quantification of GFP-positive cells by layer (%). NS: not significant. **D:** Quantification of main morphologies detected in each condition at the boundary of SVZ/IZ. **: p=0.0047 **E:** Magnifications of insets shown in A (white squares). Neuronal morphologies and neurites developed during cortical migration are shown (red arrows: bipolar neurons; blue arrows: multipolar neurons). Scale bar: 10 µm. **F:** Quantification of cell morphology (multipolar or bipolar) differentially in each layer of the cortex. **: p=0.0082, ***: p=0.0007. Student's t-test, Mann-Whitney test (700 neurons were analyzed by condition). Data represent the mean ± SEM from three independent experiments (n=4).

Supplementary Files

This is a list of supplementary files associated with this preprint. Click to download.

- SupplementaryfiguresRozeXXsetal2026.pdf